MEMS accelerometer for satellite gravimetry

Zhang, Chaoyang; Encarnação, João; Dias, Rosana A.; Hormigo, Tiago; Garcia, Ines S.; Alves, Filipe S.; Tapley, Byron

DOI
10.1016/j.asr.2025.09.009

Publication date
2025

Document Version
Final published version

Published in
Advances in Space Research

Available online at www.sciencedirect.com

ScienceDirect

Advances in Space Research 76 (2025) 5797–5813

ADVANCES IN SPACE RESEARCH (a COSPAR publication)

www.elsevier.com/locate/asr

MEMS accelerometer for satellite gravimetry

Chaoyang Zhang [a,*], João Encarnação [a,b], Rosana A. Dias [c], Tiago Hormigo [d], Ines S. Garcia [c], Filipe S. Alves [c], Byron Tapley [a]

[a] University of Texas at Austin, USA
[b] Delft University of Technology, Netherlands
[c] International Iberian Nanotechnology Laboratory, Portugal
[d] Spin.Works S.A., Portugal

Received 11 March 2025; received in revised form 25 August 2025; accepted 2 September 2025
Available online 15 September 2025

Abstract

Estimates of Earth's gravity temporal variations by GRACE(−FO) have catalyzed a wide range of scientific studies and discoveries. Although an increase in the satellite pairs would reduce the error and increase the temporal and spatial resolution, mission costs limit populating additional GRACE-like pairs. One viable solution is to reduce costs by miniaturizing the satellite. As a first step in reaching this objective, the Miniaturized Prototype for GRavity field Assessment using Distributed Earth-orbiting assets (uPGRADE) project aims to produce a CHAMP-like prototype gravimetry satellite that includes star trackers, GNSS and accelerometers in CubeSat size. As one of the primary payloads, the utility of high-precision Micro-Electro-Mechanical Systems (MEMS) accelerometer for gravimetric mission has not been considered. Here, we evaluated three, six and nine MEMS arrangements. We found that the six MEMS parallel arrangement can observe both the desired non-gravitational accelerations and additional absolute value of the angular velocity. We developed a measurement error model, associated with MEMS position and orientation errors, to guide the MEMS optimal design and assembly. Finally, we conducted uPGRADE mission simulations using appropriate observations and model errors. The impact of a 10 nm/s^2 MEMS accelerometer error on gravity recovery is very close to that of the 5 mm GNSS error. However, the accelerometer error degrades the low-degree coefficients more significantly, particularly C_{20} and C_{30}. The simulations indicate that the temporal gravity can be estimated up to degree 15, albeit with some compromise in the low-degree coefficients. Recommendations are made to lower the projected noise floor of MEMS accelerometer to enhance the low-degree coefficients accuracy.

Keywords: MEMS accelerometer; Temporal gravity; Non-conservative force; Satellite gravimetry; CubeSat

1. Introduction

Since 2000, a series of dedicated satellite gravimetry missions have been launched. The pioneer CHAMP (Challenging Minisatellite Payload, 2000–2010) mission used the high-low (GNSS to LEO) satellite to satellite tracking (hl-SST) data to retrieve Earth's gravity information, which significantly improved our knowledge of long wavelength static gravity field and provided us with a first glance at the Earth's temporal gravity, although only at very spare resolutions (Reigber et al., 2003; Weigelt et al., 2013; Flechtner et al., 2021). The GOCE (Gravity Field and Steady-State Ocean Circulation Explorer, 2009–2013) mission, equipped with a gradiometer, further pushed our boundary on global static gravity to higher resolution (Rummel and Gruber, 2010; Pail et al., 2011; Brockmann et al., 2021). The GRACE (Gravity Recovery And Climate Experiment) mission (Tapley et al., 2004), which launched two years after CHAMP and lasted until 2017, as well as

* Corresponding author.
E-mail address: CY_Zhang@austin.utexas.edu (C. Zhang).

https://doi.org/10.1016/j.asr.2025.09.009

GRACE Follow-On mission (Landerer et al., 2020), has allowed a major improvement in the mean gravity field and, more significantly, initiated a new era where temporal gravity can be observed accurately at roughly 300 km resolution globally using low-low satellite to satellite tracking (ll-SST) data. Since temporal gravity variations are induced by the movement of mass, mainly water, on Earth's surface, they are key measurements for interdisciplinary climate studies (e.g. Pail et al., 2015). The terrestrial water storage inferred from temporal gravity has been established as an Essential Climate Variable (Zemp et al., 2022). The GRACE Mass Change Measurement was designated as one of the essential observables in the National Academies 2017 Decadal Survey (Wiese et al., 2022). GRACE and GRACE-FO (here after GRACE(−FO)) have produced an invaluable global climate data record, observing mass transport of the Earth's atmosphere–ocean-solid Earth-cryosphere-hydrosphere system and their interactions over the last two decades, at a monthly sampling rate (Tapley et al., 2019). The inter-mission gap between GRACE and GRACE-FO left a one-year data gap in the gravimetric climate record. The three-satellite Swarm mission (hl-SST or similar to CHAMP), although with a lower resolution, has been used to augment the data gap and study the climate impact on our Earth system (Teixeira da Encarnação et al., 2020; Zhang et al., 2021). More recently, the Chinese gravimetric mission (ChiGaM), which adopted a GRACE-like configuration for observing temporal gravity, was launched at the end of 2021 (Xiao et al., 2023).

Although the temporal gravity collected with the ll-SST measurement principle adopted for the GRACE-type missions has high accuracy and enabled a wide range of scientific studies and discoveries, the current ll-SST missions are subject to the temporal aliasing effects and requirements for increased spatial and temporal resolutions. This issue is due to the under-sampled high-frequency mass changes, such as non-tidal ocean and atmosphere variations that are not well modeled, which result in high correlation error in some of the medium to high order spherical harmonic coefficients (Flechtner et al., 2021; Chen et al., 2022). Temporal aliasing has become the main limitation for the science return for future ll-SST gravimetric satellite missions. Increasing the number of satellites can overcome this issue (Wiese et al., 2021; Wiese et al., 2022). However, the cost of current GRACE-type satellites is too high to mass-produce (Smith, 2018; National Academies of Sciences, Engineering, and Medicine, 2019). One viable solution is to miniaturize the satellite and reduce the cost. Yunck et al. (2022) presented a conceptualized miniaturized GRACE-type satellite constellation that could be used to observe sub-daily mass variation, though this approach was not adopted for the Mass Change mission (now as GRACE-Continuity mission, e.g. Bender et al., 2025) due to high costs and technological immaturity (Wiese, 2020). Although, to date all single satellite approaches (hl-SST) have been unable to achieve the GRACE dual satellite (ll-SST) measurement accuracy, hl-SST approaches, such as the past CHAMP and ongoing Swarm missions, can still provide low resolution (300 km vs 1200 km), large scale temporal gravity for regional studies (Weigelt et al., 2013; Teixeira da Encarnação et al., 2020; Zhang et al., 2021). A constellation with a sufficiently large number of hl-SST satellites can further enhance accuracy and measure the high-frequency mass changes (Zhou et al., 2020).

In this context, as a first step in reaching miniaturized gravimetric satellites in CubeSat size, the Miniaturized Prototype for GRavity field Assessment using Distributed Earth-orbiting assets (uPGRADE) project aims to produce a prototype hl-SST gravimetry satellite in 6-U ($1U = 10 \times 10 \times 10\ cm^3$), with the objective of lowering the overall mission implementation cost (Esteves et al., 2022). The uPGRADE mission concept is focused on a single satellite technology development and demonstration, where the measurement concept is a miniaturized version of the CHAMP mission. In this concept, the primary instrument complement will be a CubeSat compatible triad of the high accuracy global positioning receiver (GNSS) for orbit determination, star trackers (SCA) for attitude determination and MEMS accelerometers (ACC) for determination of the non-gravitational acceleration acting on the satellite.

As one of the primary payloads, high-precision accelerometers are essential for the gravimetry mission to measure non-gravitational accelerations. The small size of CubeSat makes it impossible to utilize classical electrostatic accelerometers used by all previous and current gravimetry satellites (Rodrigues et al., 2022) due to their size and weight (Hines et al., 2022; Pfaffenzeller and Pail, 2023), though the newly proposed electrostatic accelerometer CubeSTAR (in 1U) may change the situation in the future (Boulanger et al., 2024). Micro-electromechanical systems (MEMS) accelerometers are more suitable for CubeSat because of their lower cost, lower power consumption, smaller size, and lightweight (Esteves et al., 2022; Hines et al., 2022). MEMS accelerometers can be based on a measurement principle that is different from the ordinary capacitive accelerometers, where the acceleration or the displacement of test mass is translated to a measurable capacitance. The proposed uPGRADE MEMS accelerometers (Esteves et al., 2022) measure the time it takes for the proof mass to be attracted towards fixed electrodes when a precisely defined voltage step is applied (higher than the threshold pull-in voltage), in the measurement principle called pull-in time (Yang et al., 2005; Garcia, 2019). Alternatively, there is also the option of optically determining the position of the proof mass with interferometry (Bao et al., 2016; Hines et al., 2022). Although the common commercial off-the-shelf MEMS accelerometers are unable to provide geodetic grade accuracy, i.e., better than 100 nm/s^2 at frequencies below a few mHz, the recent MEMS accelerometer developments are showing promising results. Pike et al. (2016) introduced the planetary microseismometer with 3 nm/s^2 accuracy between 0.1–1 Hz, which was used by the Mars InSight mission. Garcia (2019) showed that a pull-in time MEMS accelerometer has the potential

to reach 100 nm/s^2 accuracy, given that we can measure the time with ~20 ns resolution. Wang et al. (2021) presented three-axis MEMS accelerometers that reach ~100 nm/s^2 accuracy between 10–100 mHz. Hines et al. (2020, 2022) discussed a novel optomechanical accelerometers. They projected that the noise floor would be comparable to GRACE and GRACE-FO accelerometers but would be smaller (around 1 U) and lighter (~0.3 kg). It was recommended that optomechanical accelerometers can be used for future gravimetric missions and at least serve as risk-reduction devices. A similar optomechanical accelerometers (Guzman and Sanjuan, 2024) has also been proposed to aboard the Gravitational Reference Advanced Technology Test In Space (GRATTIS, Conklin et al., 2025) as one of the technology demonstration instruments. The ongoing uPGRADE mission will adopt pull-in time MEMS accelerometers (Garcia et al., 2022). The pull-in time sensitivity, noise level and long-term stability are currently under investigation (Esteves et al., 2022).

Compared to the well-established electrostatic accelerometer, which can directly output linear accelerations in all three directions, each MEMS accelerometer is usually limited to observing linear accelerations in one direction. Therefore, at least 3 MEMS accelerometers are required to measure non-gravitational accelerations in all three directions. To our knowledge, there is no relevant publication on the utility of MEMS accelerometers on a gravimetric mission. Therefore, we intend to fill this gap to provide insights for the gravimetric mission uPGRADE. In this study, we consider the MEMS accelerometer performance and focus on the following questions: 1) How many MEMS accelerometers do we need to measure non-gravitational accelerations accurately? 2) What are the useful physical arrangements of the MEMS accelerometers? 3) What are the pros and cons of these arrangements? 4) What are the maximum acceptable position and orientation errors of the MEMS accelerometers due to manufacturing imperfections? 5) What can we achieve from a gravimetric satellite like the uPGRADE mission based on our projected MEMS accelerometer accuracy?

2. The dynamics of the onboard MEMS accelerometer

The classical electrostatic accelerometers that are used for all previous gravimetric satellites are placed at the center of mass and can output the vector of non-gravitational accelerations. In consideration here, the vector acceleration is obtained by using single accelerometers placed on each of the three orthogonal satellite reference axes. The minimum number of individual accelerometers would be three. The onboard MEMS accelerometer will sense more than just the targeted non-gravitational accelerations, for instance, rotation related accelerations. Thus, to motivate the study and for the completeness of the discussion, we will first review the dynamics of the onboard MEMS accelerometer in this section.

There are three reference frames (Fig. 1) involved in the accelerometer measurement: the inertial frame (i), the satellite frame (s), and the accelerometer frame(a). The relative position of the accelerometer in the inertial frame can be expressed as

$$r^i_{acc} - r^i_{sat} = b^i = C^i_s b^s, \tag{1}$$

where b^i is the position of the accelerometer relative to the satellite center of mass, r^i_{acc} is the position of the accelerometer in the inertial frame, r^i_{sat} is the position of the satellite and C^i_s is the rotation matrix from the s-frame to the i-frame. By taking the time derivative on Eq. (1), with $\dot{C}^i_s = -\Omega^i_{si} C^i_s = C^i_s \Omega^s_{is}$ and $\dot{b}^s = 0$, we get

$$C^i_s \Omega^s_{is} b^s = \dot{r}^i_{acc} - \dot{r}^i_{sat}, \tag{2}$$

where

$$\Omega^s_{is} = \omega^s_{is}\times, \omega^s_{is} = \left[\omega_x \omega_y \omega_z\right]^T and \Omega^s_{is} = \begin{bmatrix} 0 & -\omega_z & \omega_y \\ \omega_z & 0 & -\omega_x \\ -\omega_y & \omega_x & 0 \end{bmatrix}.$$

The symbol ω^s_{is} is the angular velocity of the s-frame relative to the i-frame with coordinates in the s-frame, and the operator $\times$ stands for the vector cross product (Jekeli, 2001).

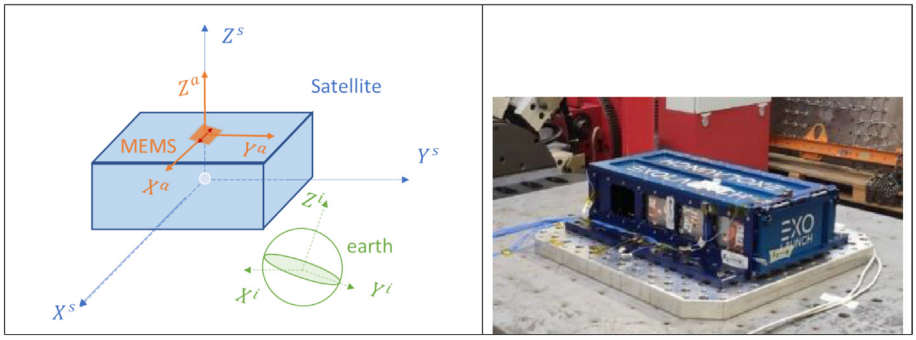

Fig. 1. Sketch of the three reference frames. The geocentric inertial frame (denoted as *i*) is in **green**. The origin of satellite frame (denoted as *s*) is at the Center of Mass (CoM, white dot). The X^s axis is generally in the velocity direction (along-track), Y^s is perpendicular to the orbital plane (cross-track) and Z^s axis forms the right-hand system that roughly points to the radial direction. The origin of the MEMS accelerometer frame (denoted as *a*) is at the center of the proof mass (**orange**). X^a axis is the sensing direction (**red** arrow), Y^a is perpendicular to X^a in the chip plane and Z^a is normal to the chip plane.

The dynamic equation of the accelerometer is given by applying a second time differentiation on Eq. (2):

$$\ddot{r}^i_{acc} = \ddot{r}^i_{sat} + \left(C^i_s \Omega^s_{is}\Omega^s_{is} + C^i_s \dot{\Omega}^s_{is}\right) b^s.$$

Splitting the total acceleration into gravitational acceleration and non-gravitational acceleration with $\ddot{r}^i_{acc} = g^i_{acc} + a^i_{acc}, \ddot{r}^i_{sat} = g^i_{sat} + a^i_{sat}$, we reach

$$a^i_{acc} = g^i_{sat} - g^i_{acc} + a^i_{sat} + \left(C^i_s \Omega^s_{is}\Omega^s_{is} + C^i_s \dot{\Omega}^s_{is}\right) b^s. \quad (3)$$

If we expand the g^i_{acc} term as a Taylor series up to the first term, we have the gravity difference (gradient) term as

$$g^i_{sat} - g^i_{acc} = g^i_{sat} - \left(g^i_{sat} + \frac{dg^i_{sat}}{dr^i_{sat}} b^i\right) = -\frac{dg^i_{sat}}{dr^i_{sat}} b^i, \quad (4)$$

where $\frac{dg^i_{sat}}{dr^i_{sat}}$ is the derivative with respect to x, y and z directions, yielding the gravity gradient tensor G^i_{sat}.

Combining Eqs. (3) and (4), we have our final dynamic equation of the accelerometer in the inertial frame

$$a^i_{acc} = a^i_{sat} + \left(C^i_s \Omega^s_{is}\Omega^s_{is} + C^i_s \dot{\Omega}^s_{is}\right) b^s - G^i_{sat} b^i. \quad (5)$$

Given the rotation matrix from the inertial frame to the satellite frame as C^s_i, we define the dynamic equation of accelerometer in the satellite frame as:

$$a^s_{acc} = C^s_i a^i_{acc} = a^s_{sat} + \left(\Omega^s_{is}\Omega^s_{is} + \dot{\Omega}^s_{is}\right) b^s - C^s_i G^i_{sat} C^i_s b^s. \quad (6)$$

3. MEMS arrangement

Each MEMS accelerometer primarily observes non-gravitational accelerations. However, it is also sensitive to centrifugal accelerations ($\Omega^s_{is}\Omega^s_{is} b^s$) and tangential accelerations ($\dot{\Omega}^s_{is} b^s$) (Eq. (6)). The Coriolis accelerations are not considered because we assume the accelerometers do not move relative to the Center of Mass (CoM). Additionally, there is also acceleration due to the gravity gradient G_{sat} since the accelerometer is not at the satellite CoM. For the sake of clarity, from here on, we name these accelerations as frame accelerations.

One MEMS accelerometer can observe a single direction only. The bare minimum of 3 orthogonally mounted MEMS accelerometers is required to observe all three directions, assuming we would be able to measure or model the frame accelerations. Eq. (6) suggests that if we place a pair of sensors symmetrically with respect to the satellite CoM, we will get the same frame accelerations but with opposite signs. With additional MEMS, we may be able to isolate the non-gravitational accelerations and also acquire attitude information. In this section, we will discuss three scenarios with the arrangement of 3, 6 and 9 MEMS, which have different applications and sensitivities.

3.1. Three MEMS

With only 3 MEMS, we need to arrange them orthogonally to be able to be sensitive to the three-dimensional nature of the non-gravitational accelerations. Each of the MEMS accelerometers senses one direction in the satellite frame (e.g., Fig. 2a) and observes all components of the accelerations as indicated in Eq. (6). Other than the non-gravitational accelerations, the instrument will also observe the frame accelerations. Therefore, 3 MEMS alone are unable to directly measure the non-gravitational accelerations without the aid of additional information, notably attitude sensors.

The frame accelerations are all proportional to the distance between the satellite CoM and the MEMS proof mass. Therefore, it is beneficial to arrange the 3 MEMS as close as possible to the satellite CoM to minimize them. Fig. 2a presents one possible MEMS arrangement that meets this criterion. The A_{x_1} MEMS is placed at the satellite CoM at the X^sY^s plane and senses the X^s direction (Tab. 1). A_{y_1} is on the same wafer as A_{x_1} and is sensing the Y^s direction. It is important to maximize the number of MEMS accelerometers in the same wafer because the relative positioning is much more accurate when etching multiple micro-machines in the same wafer compared to assembling separate ones. A_{z_1} is along the Z^s axis and perpendicular to the X^sY^s plane and is sensing the Z^s direction.

Only considering the degree zero term of Earth's gravity (or "point-mass" Earth) $g^i_{sat} = \frac{GM}{(r^i_{sat})^2}$, the magnitude of gravity gradient term can be approximated to $\approx 2|g^i_{sat}|\frac{|b^i|}{|r^i_{sat}|}$ where GM is Earth's gravitational constant. Usually, the accelerometers are several centimeters away from satellite CoM (the size of one MEMS is roughly 2 cm × 2 cm). Assuming a 5 cm offset and 450 km altitude, the magnitude of gravity gradient term is $\sim 10^{-7}$ m/s^2, which is within the potential measurement accuracy of MEMS accelerometers. Other higher degree and order non-spherical gravity effects are more than three orders of magnitude smaller than the degree zero term. They can be neglected under the current MEMS measurement accuracy. Since the total mass of Earth does not change over time, with a good knowledge of satellite position from GNSS and attitude from star camera, we would be able to compute this term. From here on, we will not consider the gravity gradient term in our analysis.

The tangential acceleration is perpendicular to the coordinate axes. Therefore, if we align the sensing direction of MEMS with each of the satellite coordinate axes, we can reduce the effect of the angular accelerations induced tangential force. However, we will still need precise attitude information to remove the centrifugal acceleration, which acts parallel to the coordinate axes. The angular velocity is usually smaller than 1.2 mrad/s, which takes place in the pitch direction as a result of the nominal Earth-pointing mode as the satellite orbits the Earth at Low Earth Orbit (LEO). If we consider the centrifugal acceleration in a general form of $\omega^2 x$, with rotational rate ω and distance to CoM x (a few centimeters), the angular velocity

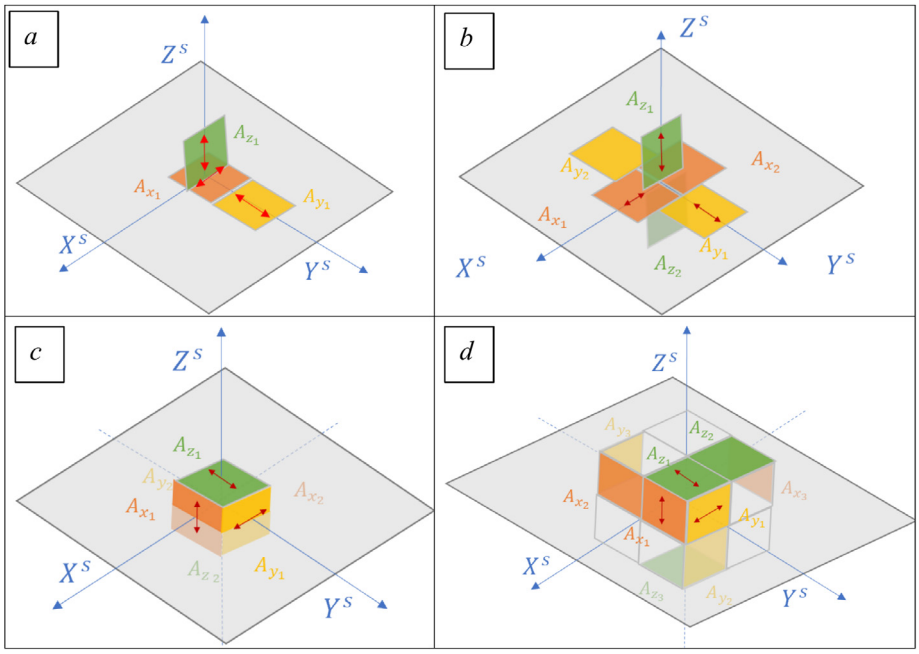

Fig. 2. MEMS arrangements a) 3 MEMS case, b) 6 MEMS parallel case, where each MEMS sensing direction is along the corresponding axis, c) 6 MEMS perpendicular case, where the sensing direction is perpendicular to the axis, and d) 9 MEMS case. MEMS devices are colored squares in **orange** (along the X^s axis) named A_{x_i}, **yellow** (along the Y^s axis) named A_{y_i} and **green** (along the Z^s axis) named A_{z_i}. **The red arrow highlights the sensing direction of the MEMS device**. The **gray** rectangle indicates the X^sY^s plane of the satellite frame.

observation accuracy needs to be better than 0.1 mrad/s (or ~10 arcsec/s) to maintain a~10^{-9} m/s^{2}accuracy in centrifugal acceleration estimation.

Although a 3 MEMS configuration is always not preferred, since it requires additional attitude observation, the discussion here ensures that it is still possible to observe the non-gravitational accelerations in the extreme scenario that we have a failure of one MEMS in a six or more MEMS configuration.

3.2. Six MEMS

The magnitude of the frame accelerations depends on the location of the MEMS. As such, it is possible to take advantage of this fact and place two MEMS symmetrically relative to satellite CoM to ensure they experience equal frame accelerations with opposite signs. With 6 MEMS, it is possible to combine them into three pairs with each pair sensing one of the 3 orthogonal directions. Fig. 2b and 2c depict two such arrangements. In the parallel case (Fig. 2b), the MEMS sensing direction is along the corresponding axes while in the perpendicular case (Fig. 2c), the sensing direction is perpendicular to the axes. For instance, in the parallel case, MEMS A_{x_1} and A_{x_2} are on the X^s axis and observe the accelerations in the X^s direction. They are placed 1 cm away from the CoM on the two sides of the axis, symmetrically (see Fig. 2b and Table 1). The total acceleration observed by each of those MEMS accelerometers can be written as:

$$\begin{cases} A^s_{x_1} = a^s_x - \left(\omega^s_{is_z}\right)^2 \cdot \rho_{x_1} - \left(\omega^s_{is_y}\right)^2 \cdot \rho_{x_1} \\ A^s_{x_2} = a^s_x + \left(\omega^s_{is_z}\right)^2 \cdot \rho_{x_2} + \left(\omega^s_{is_y}\right)^2 \cdot \rho_{x_2} \\ A^s_{y_1} = a^s_y - \left(\omega^s_{is_z}\right)^2 \cdot \rho_{y_1} - \left(\omega^s_{is_x}\right)^2 \cdot \rho_{y_1} \\ A^s_{y_2} = a^s_y + \left(\omega^s_{is_z}\right)^2 \cdot \rho_{y_2} + \left(\omega^s_{is_x}\right)^2 \cdot \rho_{y_2} \\ A^s_{z_1} = a^s_z - \left(\omega^s_{is_x}\right)^2 \cdot \rho_{z_1} - \left(\omega^s_{is_y}\right)^2 \cdot \rho_{z_1} \\ A^s_{z_2} = a^s_z + \left(\omega^s_{is_x}\right)^2 \cdot \rho_{z_2} + \left(\omega^s_{is_y}\right)^2 \cdot \rho_{z_2} \end{cases} . \tag{7}$$

where $A^s_{n_i}$ is the acceleration observed by the A_{n_i} MEMS accelerometer, with n = x, y or z and i = 1,2 or 3, e.g., $A^s_{x_1}$ is the acceleration observed by the A_{x_1} MEMS in the satellite frame, a^s_x is the satellite non-gravitational acceleration in the X direction, $\omega^s_{is_z}$ the z component of the angular velocity, ρ_{x_1} the distance between the A_{x_1} MEMS sensing head and satellite CoM.

Given $\rho = \rho_{x_1} = \rho_{x_2} = \frac{1}{2}\rho_{y_1} = \frac{1}{2}\rho_{y_2} = \rho_{z_1} = \rho_{z_2}$ (Table 1), the sum of each of the three MEMS pairs (also called common mode, e.g. Frommknecht et al., 2011) yields the desired non-gravitational accelerations of the satellite (Eq. (8a)).

$$\begin{cases} a^s_x = \frac{1}{2}\left(A^s_{x_1} + A^s_{x_2}\right) \\ a^s_y = \frac{1}{2}\left(A^s_{y_1} + A^s_{y_2}\right) \\ a^s_z = \frac{1}{2}\left(A^s_{z_1} + A^s_{z_2}\right) \end{cases} . \tag{8a}$$

Table 1
The orientation and position of each MEMS in the 3 MEMS, 6 MEMS, or 9 MEMS arrangement (Fig. 2).

MEMS name	3 MEMS case (Fig. 2a)	
	Orientation	Position (s-frame) [cm]
A_{x_1}	Along the X^s axis, observe X^s	[0 0 0]
A_{y_1}	Along the Y^s axis, observe Y^s	[0 2 0]
A_{z_1}	Along the Z^s axis, observe Z^s	[0 0 1]
	6 MEMS parallel case (Fig. 2b)	
	Orientation	Position (s-frame) [cm]
$A_{x_1}\|A_{x_2}$	Along the X^s axis, observe X^s	[1 0 0] | [-1 0 0]
$A_{y_1}\|A_{y_2}$	Along the Y^s axis, observe Y^s	[0 2 0] | [0 −2 0]
$A_{z_1}\|A_{z_2}$	Along the Z^s axis, observe Z^s	[0 0 1] | [0 0 −1]
	6 MEMS perpendicular case (Fig. 2c)	
	Orientation	Position (s-frame) [cm]
$A_{x_1}\|A_{x_2}$	Perpendicular to the X^s axis, observe Z^s	[1 0 0] | [−1 0 0]
$A_{y_1}\|A_{y_2}$	Perpendicular to the Y^s axis, observe X^s	[0 1 0] | [0 −1 0]
$A_{z_1}\|A_{z_2}$	Perpendicular to the Z^s axis, observe Y^s	[0 0 1] | [0 0 −1]
	9 MEMS case (Fig. 2d)	
	Orientation	Position (s-frame) [cm]
$A_{x_1}\|A_{x_2}\|A_{x_3}$	Perpendicular to the X^s axis, observe Z^s	[2 1 1] | [2 −1 1] | [−2 1 1]
$A_{y_1}\|A_{y_2}\|A_{y_3}$	Perpendicular to the Y^s axis, observe X^s	[1 2 1] | [1 2 −1] | [1 −2 1]
$A_{z_1}\|A_{z_2}\|A_{z_3}$	Perpendicular to the Z^s axis, observe Y^s	[1 1 2] | [−1 1 2] | [1 1 −2]

$$\begin{cases} \left(\omega^s_{Si_x}\right)^2 = -\frac{1}{8\rho}\left\{2\left(A^s_{x_2}-A^s_{x_1}\right)-\left(A^s_{y_2}-A^s_{y_1}\right)-2\left(A^s_{z_2}-A^s_{z_1}\right)\right\} \\ \left(\omega^s_{Si_y}\right)^2 = \frac{1}{8\rho}\left\{2\left(A^s_{x_2}-A^s_{x_1}\right)-\left(A^s_{y_2}-A^s_{y_1}\right)+2\left(A^s_{z_2}-A^s_{z_1}\right)\right\} \\ \left(\omega^s_{Si_y}\right)^2 = \frac{1}{8\rho}\left\{2\left(A^s_{x_2}-A^s_{x_1}\right)+\left(A^s_{y_2}-A^s_{y_1}\right)-2\left(A^s_{z_2}-A^s_{z_1}\right)\right\} \end{cases} . \tag{8b}$$

The subtraction of the three MEMS pairs (also called differential mode) results in three unknown quadratic angular velocity terms. The combinations of those three equations yield the absolute quantity of the angular velocities (Eq. (8b)). Those bonus observables are another advantage of using 6 MEMS devices. They could be used to augment the star camera observed satellite attitude via data fusion (e.g., Klinger, 2018; Harvey and Sakumura, 2019; Harvey et al., 2022). We should also note that we might encounter numerical problems resulting from the MEMS observation noise, where the quadratic angular velocity may have a negative value, since there is no quadratic exponent on the right side of Equation (8b). However, from an alternative point of view, the negative values reflect the partial absolute error of the MEMS observation noise. They may bring a new way to understand MEMS error characteristics.

The common mode of the 6 MEMS perpendicular case (Fig. 2c) is similar to the parallel case, which yields the targeted non-gravitational accelerations (Eq. A(2). The differential mode yields three equations that contain 6 unknown parameters (Eq. A(3). Thus, we cannot obtain additional attitude-related information from this arrangement. Additionally, from an engineering point of view, the construction of the perpendicular case is of higher complexity. In the parallel case, the four horizontal MEMS (namely $A_{x_1}, A_{x_2}, A_{y_1}$ and A_{y_2}) can be embedded in one wafer and the other two in a second wafer, while in the perpendicular case, all 6 MEMS are separated and split into 6 planes, which requires high accuracy in orthogonal mounting and dramatically increases the construction complexity. Therefore, the parallel case (Fig. 2b) is preferred under the current uPGRADE project. We should also note that the perpendicular case (Fig. 2c) is more compact or saves more space. It could be a better option if the project has a very tight volume budget.

3.3. Nine MEMS

Although we cannot directly obtain attitude information from the perpendicular configuration (6 MEMS), the differential mode suggests we might be able to directly isolate the angular acceleration if we can increase the number of MEMS devices to 9. There are 6 unknown parameters (Eq. A(3), within which three angular velocities are presented in product form (e.g., $\omega^s_{is_x}\cdot\omega^s_{is_z}$). Therefore, if one

MEMS accelerometer is added into each direction, the three additional equations can be used to isolate angular accelerations (3 plus an extra 3). Fig. 2d provides a possible 9 MEMS configuration that meets this requirement. The differential mode yields 6 equations (Eq. A(5). The linear combination of Equation A(5) yields angular accelerations (Eq. A(6). Usually, the star camera has higher accuracy on lower frequencies, while the MEMS accelerometers observed angular accelerations are better on higher frequencies. The angular accelerations observed by MEMS accelerometers would enhance the high-frequency components of the star camera and produce a more accurate satellite attitude. For instance, Klinger (2018) and Harvey et al. (2019, 2022) fused angular acceleration observations from the accelerometer into star camera attitude data for the GRACE and GRACE-FO attitude reconstruction. However, we note that the angular acceleration output from GRACE-type accelerometers is not pure angular acceleration but includes the contribution of the centrifugal accelerations (Klinger, 2018; Harvey et al., 2019), which is similar to the angular velocity product terms in Equation A(3).

4. Position and orientation error

We discussed a variety of MEMS configurations and their potential added values on attitude estimation. Although the 9 MEMS configuration would be ideal for the uPGRADE mission, with limitations in power, funding, and data transmission capacity, the 6 MEMS configuration is adopted. Compared to the 3 MEMS configuration, the 6 MEMS parallel configuration can directly observe the non-gravitational accelerations without the aid of star camera data. Although it cannot deliver angular acceleration as the 9 MEMS configuration, the absolute value of the angular velocity can still be retrieved.

Measuring non-gravitational accelerations is essential for including the 6 MEMS parallel configuration in the uPGRADE mission. The MEMS accelerometers may, due to the limited accuracy in the assembly process, be subject to position and orientation errors (Fig. 3). Similar discussions have also been carried out on GOCE data analysis (e.g. Stummer, 2012). The position error (Fig. 3a) is defined as the difference between the design and the actual position. Similarly, the orientation error (Fig. 3b) is the difference between the designed and the actual sensing direction. These errors will eventually propagate to the non-gravitational acceleration measurements and degrade the accuracy of the observations. In this section, we will discuss the error budget of the non-gravitational acceleration measurements due to the MEMS position and orientation errors and the associated minimum design and assembly requirements.

As discussed in the last section, the common mode of each pair of MEMS accelerometers can yield non-gravitational acceleration. Assuming one pair of MEMS (denoted as A_{x1} and A_{x2}) are placed at b_1^s and b_2^s, where b_1^s and b_2^s are symmetric with respect to satellite CoM (Fig. 3a), the total acceleration vectors at those two positions are

$$\begin{cases} A_{b_1}^s = a_o^s + \Omega_{is}^s \cdot \left(\Omega_{is}^s \cdot b_1^s\right) + \dot{\Omega}_{is}^s \cdot b_1^s \\ A_{b_2}^s = a_o^s + \Omega_{is}^s \cdot \left(\Omega_{is}^s \cdot b_2^s\right) + \dot{\Omega}_{is}^s \cdot b_2^s \end{cases}, \tag{9}$$

where $A_{b_1}^s$ and $A_{b_2}^s$ are the total acceleration at position b_1^s and b_2^s, a_o^s is the linear acceleration, and the third and fourth terms are the frame acceleration, with Ω_{is}^s as defined for Equation (2).

Replacing the frame acceleration with $B_{b_1}^s and B_{b_2}^s$, where

$$\begin{cases} B_{b_1}^s = \Omega_{is}^s \cdot \left(\Omega_{is}^s \cdot b_1^s\right) + \dot{\Omega}_{is}^s \cdot b_1^s \\ B_{b_2}^s = \Omega_{is}^s \cdot \left(\Omega_{is}^s \cdot b_2^s\right) + \dot{\Omega}_{is}^s \cdot b_2^s \end{cases},$$

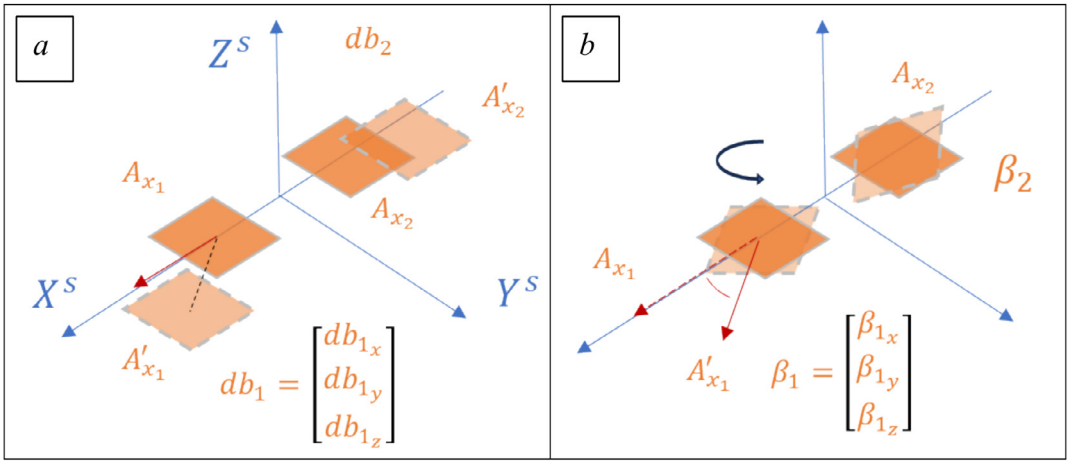

Fig. 3. MEMS accelerometers position error (a) and orientation error (b). The position error (db_1) is defined as the actual position (A'_{x_1}) of the MEMS and the designed position (A_{x_1}). Similarly, the orientation error (β_1) is the deviation of the actual sensing direction from the designed direction.

Equation (9) can be simplified to:

$$\begin{cases} A^s_{b_1} = a^s_o + B^s_{b_1}, \begin{bmatrix} A^s_{b_{1x}} \\ A^s_{b_{1y}} \\ A^s_{b_{1z}} \end{bmatrix} = \begin{bmatrix} a^s_{ox} \\ a^s_{oy} \\ a^s_{oz} \end{bmatrix} + \begin{bmatrix} B^s_{b_{1x}} \\ B^s_{b_{1y}} \\ B^s_{b_{1z}} \end{bmatrix} \\ A^s_{b_2} = a^s_o + B^s_{b_2}, \begin{bmatrix} A^s_{b_{2x}} \\ A^s_{b_{2y}} \\ A^s_{b_{2z}} \end{bmatrix} = \begin{bmatrix} a^s_{ox} \\ a^s_{oy} \\ a^s_{oz} \end{bmatrix} + \begin{bmatrix} B^s_{b_{2x}} \\ B^s_{b_{2y}} \\ B^s_{b_{2z}} \end{bmatrix} \end{cases}. \tag{10}$$

Assuming both MEMS are placed at b^s_1 and b^s_2 with no error and they both sense the X-axis in the s-frame, the common mode output of the non-gravitational acceleration in the X-axis direction is:

$$A^s_{b_{1x}} + A^s_{b_{2x}} = 2a^s_{ox}.$$

If the two MEMS are not perfectly mounted and there is an offset from the designed position with db_1 and db_2, the resulting common mode output is

$$\begin{aligned} &\overset{-s}{A}_{b_{1x}} + \overset{-s}{A}_{b_{2x}} = 2a^s_{ox} + e_1 \\ &e_1 = dB^s_{x_1} + dB^s_{x_2} = \Omega_1 \cdot \left(\Omega^s_{is} \cdot \left(db^s_1 + db^s_2\right)\right) + \dot{\Omega}_1 \cdot \left(db^s_1 + db^s_2\right) \end{aligned} \tag{11}$$

where $\overset{-s}{A}_{b_{1x}}$ and $\overset{-s}{A}_{b_{2x}}$ are MEMS measurements in their actual positions (with the offsets db_1 and db_2), e_1 is the common mode acceleration error induced by the position error, Ω_1 and $\dot{\Omega}_1$ are the first row of Ω^s_{is} and $\dot{\Omega}^s_{is}$.

As shown in Eq. (11), the imperfect positioning of the MEMS devices introduces additional frame acceleration errors. The common mode error e_1 is proportional to the sum of the position error $db_1 + db_2$. Therefore, for analysis, we use one position error value for a pair of MEMS devices, which is equivalent to saying that only one of the two MEMS is mounted with an unknown offset db^s_o.

The situation for orientation error is not as simple as for the position error. For instance, in the previous position error case, the accelerations $\overset{-s}{A}_{b_{1x}}$ and $\overset{-s}{A}_{b_{2x}}$ are still exclusively sensitive to the X-axis. However, by considering alignment errors, the MEMS accelerometer is rotated by an unknown angle in the pitch, yaw, or roll directions (β_1 and β_2), making it sensitive to accelerations from the Y and Z axes. Under the small-angle assumption, the common mode with orientation error is:

$$\begin{aligned} &\overset{\sim s}{A}_{b_{1x}} + \overset{\sim s}{A}_{b2x} = 2\ddot{r}^s_{x_1} + e_2 \\ &e_2 = -A^s_{b_{1z}}\beta_{1y} + A^s_{b_{1y}}\beta_{1z} - A^s_{b_{2z}}\beta_{2y} + A^s_{b_{2y}}\beta_{2z} \\ &= -a^s_{oz}\left(\beta_{1y} + \beta_{2y}\right) + a^s_{oy}\left(\beta_{1z} + \beta_{2z}\right) - B^s_{b_{1z}}\left(\beta_{1y} - \beta_{2y}\right) + B^s_{b_{1y}}\left(\beta_{1z} - \beta_{2z}\right) \end{aligned} \tag{12}$$

where $\overset{\sim s}{A}_{b_{1x}}$ and $\overset{\sim s}{A}_{b2x}$ are the MEMS measurements with the actual orientation (with misalignment), e_2 is the common mode acceleration error induced by the orientation error.

The acceleration error produced by misalignment (orientation error) depends on the interaction of all the four angle errors, which for the X-axis are $\beta_{1y}, \beta_{1z}, \beta_{2y}$ and β_{2z}. It would be hard to quantify the point-to-point relation between orientation error and common mode error if all four angles are set to change freely. To reduce the degree of complexity and find a good way to approximate the expression of e_2, we implemented a series of Monte Carlo experiments, where all four rotation angles were randomly selected within the same order of magnitude, e.g., all ranging from 0.1 to 0.9 and −0.9 to −0.1 in the unit of degrees. In total, 6000 sets of orientation errors are used to calculate the common mode error using GRACE L1B (Case et al., 2002), GRACE-FO L1B (Wen et al., 2019) and uPGRADE simulation data. We then computed the RMS of the common mode error for each of the 6000 realizations. It would be difficult to visualize the results considering the four angles separately. Therefore, we used the sum of the four error angles or $\beta^+ = \beta_{1y} + \beta_{2y} + \beta_{1z} + \beta_{2z}$ for the X-axis and the difference between the y and z components or $\beta^- = \beta_{1z} + \beta_{2z} - \beta_{1y} - \beta_{2y}$ for the Y-axis.

Fig. 4a shows the RMS of the common mode acceleration error using GRACE L1B attitude and non-gravitational acceleration data from 2010-01-01. The RMS of common mode error is proportional to the absolute value both β^+ and β^- (Fig. 4a). It also shows that the RMSs are symmetric with respect to the origin. Fig. 4b suggests that the profile along Y = 0 (or $\beta^- = 0$) alone has a good representation of the overall error pattern (notice the change in the Y-axis scale). In this case, the RMS of common mode error is only associated with the summation of the orientation errors. Therefore, we can further simplify our model to the situation that only one MEMS has an orientation error α while the other MEMS is in perfect orientation. Fig. 4c shows the RMS of common model error when the α ranges from (10^{-7} to 10^{-2}), which is an excellent representative of the case that all four angles are randomly chosen (Fig. 4b).

Therefore, the complex association between MEMS position and orientation error and the common mode error can be simplified to the scenario where only one MEMS of the paired MEMS has position and orientation errors. We should emphasize that those simplifications hold when we are only concerned about the magnitude of the common mode error, and we assume that each type of error is in the same order of magnitude.

In practice, we have both orientation and position errors at the same time. Fig. 5 shows the total common mode error RMS (colored pixels) with a range of orientation errors (X-axis) and position errors (Y-axis) for the parallel configuration (Fig. 2b). GRACE observed non-gravitational accelerations, and attitude data (2010-01-01) are considered. Like our previous analysis, both position and orientation errors are proportional to the RMS of common mode error, where one order of magnitude increase in position error (e.g., mm to cm) will also roughly increase the RMS by one order of magnitude (same for the orientation error). Since the error in the Y^s and Z^s direc-

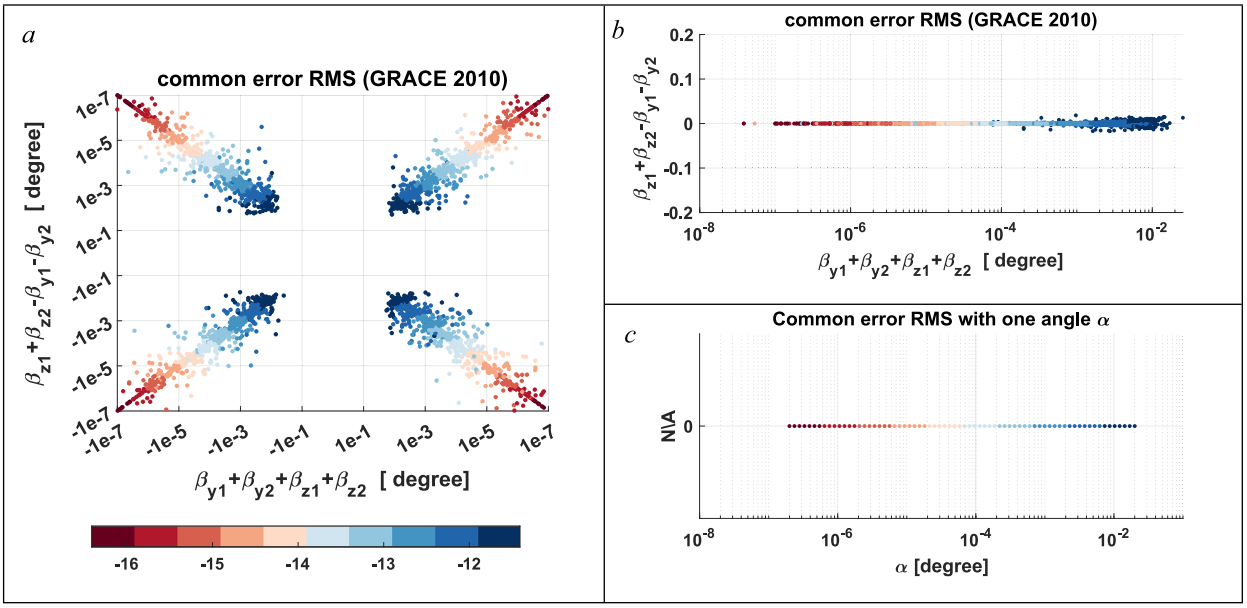

Fig. 4. Common mode error RMS in m/s^2 (log10 scaled) based on Equation (12) using GRACE L1B data (2010-10-01): a) Four angles are randomly selected, and both the X and Y-axis are in log scale, b) same as a) but the Y-axis is in linear scale, c) only one angle α is used.

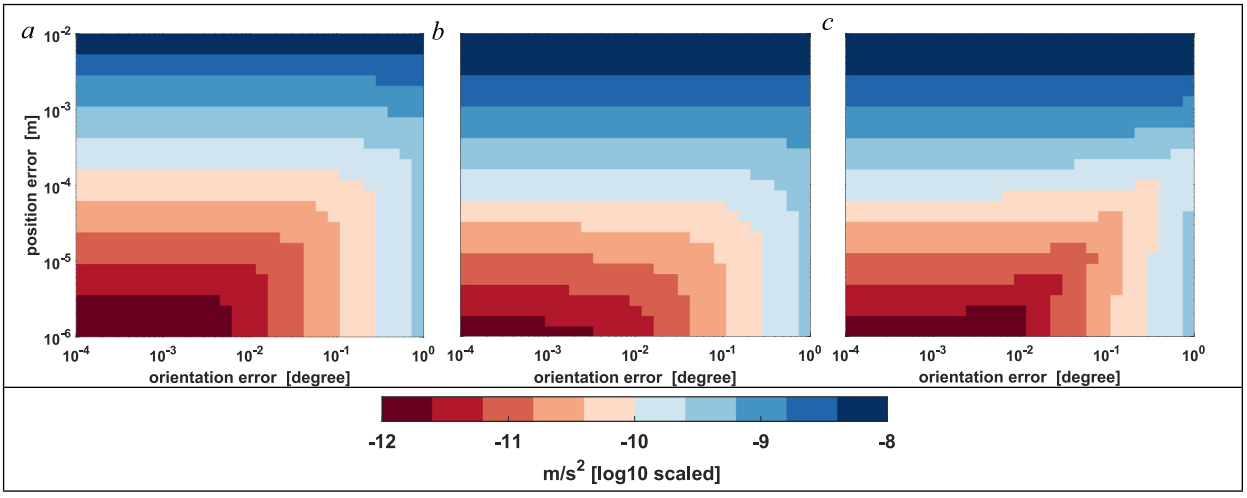

Fig. 5. RMS of the total common mode error due to position and orientation error using GRACE L1B data (2010-01-01): a) X^s axis, b) Y^s axis, and c) Z^s axis.

tions is proportional to the non-gravitational acceleration signal in the X^s-axis (e.g., Eqs. (11) and (12)), which is generally in the along-track direction with larger amplitude, their common mode errors (Fig. 5b and c) are relatively higher compared to the X^s direction (Fig. 5a), as represented with a larger blue area and smaller red area. For instance, given 0.1 degree orientation error and 0.1 mm position error, the error RMS in X^s direction is smaller than 10^{-10} m/s while that of Y^s and Z^s *directions are greater than* 10^{-10} m/s. The exact patterns may change, depending on the date we choose, such as due to different solar activity. The general pattern does not change much over time whether we use the L1B dataset from GRACE or GRACE-FO (not shown).

Since the general pattern of the common mode error RMS does not change significantly, the error analysis can also be used to guide the satellite design and determine a minimum accuracy requirement for the assembling of MEMS configuration. The orientation and position errors must not induce a common mode acceleration error larger than the observation accuracy requirement. For a minimum accuracy requirement of, for example, 0.1 nm/s^2, the MEMS configuration needs an assembly and mounting accuracy better than 0.1 mm and 0.1 degree in terms of its

position and alignment. Another lesson from the error pattern is that the efforts to improve only one component of the assembling (e.g., orientation or position) alone may fail to reduce the common mode error. For example, if the orientation error is around 0.1 degree, the improvement of position error from 0.1 mm to 1μ m does not change the overall common mode error. Instead, both error components need to be considered together. The most economical and optimal way to determine the orientation and position accuracy pair is to roughly follow along the diagonal, which may be steeper or shallower depending on the difficulty in aligning or positioning the MEMS accelerometers, respectively, since both components are at their minimum requirement for a given accuracy.

5. Simulation study

The primary scientific output of the uPGRADE is the temporal gravity solution, which is subject to the accuracy of the science instruments (notably the MEMS accelerometer and GNSS receiver) as well as the background geophysical models (notably ocean tide and non-tidal atmosphere and ocean models). Even though one would expect a higher payload accuracy to yield better temporal gravity, in reality, the quality of estimated temporal gravity can also be limited by geophysical model uncertainties, such as in ocean tide. Thus, the most efficient strategy is to avoid over-designing science payloads. In this way, we could limit the overall cost and engineering challenge while ensuring our scientific objectives.

In this section, we set up a simulation environment based on the Center for Space Research (CSR) in-house multi-satellite orbit determination program (MSODP, Rim, 1992; Kim, 2002) for the uPGRADE mission. A set of realistic instruments and model errors based on the lessons we learned from GRACE are used to quantify their potential impacts on the gravity field estimation. The results can serve as a reference for the uPGRADE (and similar mission) payloads design and development.

5.1. Setup

The simulation procedure consists of two steps: the forward modeling step and the backward inversion step. In the forward modeling step, a series of geophysical models (e.g., ocean tide model) and instrument observations (such as satellite attitude data and accelerometer data) are defined as ground truth. They are used to propagate the satellite orbit, which would be used to generate error-free GNSS observations. During the inversion step, errors will be added to the GNSS phase observations, as well as other instrument observations. Another set of geophysical models will be used as reference fields (or nominal fields) to represent the inability to know the ground truth with perfect accuracy. We follow the conventional approach of defining the model error as the difference between the models used in the forward modeling step and those used in the inversion step (Table 2). For instance, the difference between FES04 (Lyard et al., 2006) and EOT08 (Skachko et al., 2008) is defined as ocean tide model error. The non-tidal atmosphere and ocean de-aliasing (AOD) error is approximated by the difference between AOD1B-RL06 and AOD1B-RL07 (Dobslaw et al., 2017; Shihora et al., 2022). We choose the CSR mascon solution (Save et al., 2016) in spherical harmonic representation, where GGM05C has been added back (Save, 2020), as the true gravity model for the forward modeling step. The GGM05C is used as the nominal gravity model for the inversion step. In this way, we can largely minimize the commission and omission error due to the differences in the static background gravity model (Gunter et al., 2006) but also keep the fidelity of the simulation. It ensures the nominal field deviates from the true field mainly due to temporal gravity since our interest focuses more on the recoverability of temporal gravity rather than static gravity.

Initial conditions are chosen to close GRACE circular orbit (e.g. GNV1B product, Case et al., 2010) with a 500 km altitude and 89 degree inclination and used to propagate the simulated uPGRADE satellite orbit. GNSS phase measurements (30-second sampling rate) are the primary observations in this simulation, the same as what is used in the CSR GRACE GNSS data processing (Pie et al., 2021). Four phase observations between two GNSS satellites and uPGRADE satellites, as well as one ground station, are used to form the classical double-differenced observations (Rim, 1992). This observation combination strategy can help reduce the common error and eliminate the receiver clock error. In this simulation study, we choose 5 mm and 1 cm (standard deviation) white noise as a lower

Table 2
List of background models and force models that are used for forward propagation and inversion.

Model/observations	Forward Modeling (Truth)	Backward Inversion
Static background field	CSR mascon solution	GGM05C
Ocean tide	FES04	EOT08
AOD	AOD1B 06	AOD1B 07
Star camera	Nominal satellite orientation	Nominal satellite orientation + white error
Accelerometers	Modeled non-gravitational accelerations	Modeled non-gravitational accelerations + colored error
GNSS observations	Double differences	Double differences + white error

bound and upper bound of the GNSS double-differenced observation error. As a comparison, GRACE and GRACE-FO real data processing usually results in a phase RMS at the level of around 4 mm to 8 mm (Kang et al. 2006, 2020).

We use the simulated satellite nominal orientation as the true satellite attitude, which is defined by the velocity (along-track) direction, the radial direction and the cross-track direction. The GRACE attitude observation is more accurate in roll direction (~30 μrad) and less sensitive in the other two directions (~200 μrad). The uPGRADE satellite will have two star trackers, which is similar to the GRACE satellite configuration. Conservatively, 100 μrad (~20 arcsec) white noise is used to corrupt the "true" attitude and generate attitude observation. Although the differential mode of the 6 MEMS configuration can yield additional attitude information, attitude uncertainty is not the dominant error sources in uPGRADE simulation. In this simulation, its potential contribution is not included in the discussion.

Atmosphere drag, solar radiation pressure, Earth radiation pressure modeled in orbit propagation (Kim, 2000) are set to be the true non-gravitational acceleration. UPGRADE MEMS devices are currently under development and are anticipated to achieve an accuracy of 10 nm/s^2 to 100 nm/s^2 within the measurement band. As a comparison, the sensitive direction of the GRACE accelerometer (e.g. along-track) and the less sensitive direction (e.g. cross-track) are in the order of 0.1 nm/s^2 and 1 nm/s^2. The orientation and positioning error induced acceleration error is 2–3 orders of magnitude smaller than the MEMS noise level, giving the manageable submillimeter and one tenth of degree positioning and orientation precision. We will not consider their contribution here. In this simulation, we used a PSD model similar to that defined by Kim (2000) and Kim and Tapley (2002)

$$PSD = \left(1 + \frac{0.001}{f}\right) \times \gamma \mathrm{m}^2/\mathrm{s}^4/Hz \tag{13}$$

where f is frequency, and γ is "floor" variance. Two different values for γ are used to generate high noise ($\gamma^+ = 10^{-14}$) and low noise ($\gamma^- = 10^{-16}$). They represent the aforementioned 100 nm/s^2 and 10 nm/s^2 cases respectively. Readers are referred to Appendix B for how we generate colored noise and an example of the noise realization.

5.2. Simulation result

The Earth's geopotential is represented in the form of spherical harmonic expansion (Heiskanen and Moritz, 1967; Hofmann-Wellenhof and Moritz, 2006)

$$V(r,\theta,\lambda) = \frac{GM}{a}\sum_{n=0}^{\infty}\sum_{m=0}^{n}\left(\frac{a}{r}\right)^{n+1}\left(\bar{C}_{nm}cosm\lambda + \bar{S}_{nm}sinm\lambda\right)\bar{P}_{nm}(cos\theta), \tag{14}$$

where r is the radial distance from the geocenter; θ is the co-latitude; λ is the longitude; GM is gravity constant; a is the semi-major axis of the reference ellipsoid; $\bar{C}_{nm}$ and $\bar{S}_{nm}$ are the fully normalized geopotential coefficients (or Stokes coefficients) per degree n and order m; $\bar{P}_{nm}$ is fully normalized Legendre function. We use the residual degree variance (DV, in terms of geoid height) to measure the gravity error associated with different instruments or geophysical model errors (Eq. (15)).

$$DV_n = a \cdot \sqrt{\sum_{m=0}^{n}\left(d\bar{C}_{nm}^{2} + d\bar{S}_{nm}^{2}\right)}, \tag{15}$$

where $d\bar{C}_{nm} and d\bar{S}_{nm}$ are the residual geopotential coefficients between the true gravity field and the recovered gravity field (i.e., the one obtained from the inversion step). The degree variance measures the error amplitude at a specific degree or a specific spatial resolution. For instance, degree 20 roughly represents 1000 km resolution at the equator.

There are 2 model errors and 3 instrument errors (two cases each). Fig. 6a summarizes the impact of each error source (in total 8) on the temporal gravity recovery quality for August 2008. All solutions are solved up to degree and order (d/o) 40. For comparison, we use the standard deviation of CSR GRACE mascon solutions (Save et al., 2016) to represent the power of real-world temporal gravity (brown line with dot in Fig. 6a and 6b). If the error curve is below the mascon curve, we predict the temporal signal could be well observed up to that degree. If the error curve is above the mascon curve, it may not be able to fully recover the signals associated with those degrees. We define 1 order of magnitude difference between the error curve and signal curve as our threshold of recoverability (e.g. Bezděk et al., 2016; Zhang et al., 2021). For instance, if the error curve is one order of magnitude higher than the signal (mascon) curve at degree x, we consider degree x as our maximum recoverable degree. This criterion will be used to quantify the effect of each error source on the gravity recovery.

The simulation result suggests that the GNSS observation error is one of the largest error sources (Fig. 6a, red line with square), which agrees with the previous studies (e.g., Zhou et al., 2020). A 5 mm GNSS phase error will restrict the recovery to only degree 15. The attitude observation error (Fig. 6a, blue), on the other hand, has the least effect on gravity recovery. Even the relatively high noise (100 μrad or ~ 20 arcsec) results in a gravity error that is two orders of magnitude smaller than that of the 5 mm GNSS phase noise. However, we should recall that a higher accuracy attitude observation can be of great value in the worst-case scenario where we would only have one MEMS working in one certain direction (see section 3.1). The impact of the MEMS accelerometers error on gravity recovery is more prominent (Fig. 6a, green with cross) as compared to other simulation studies (e.g. Zhou et al., 2020; Pfaffenzeller and Pail, 2023), where GRACE grade (or better) accelerometers are assumed. Because the MEMS

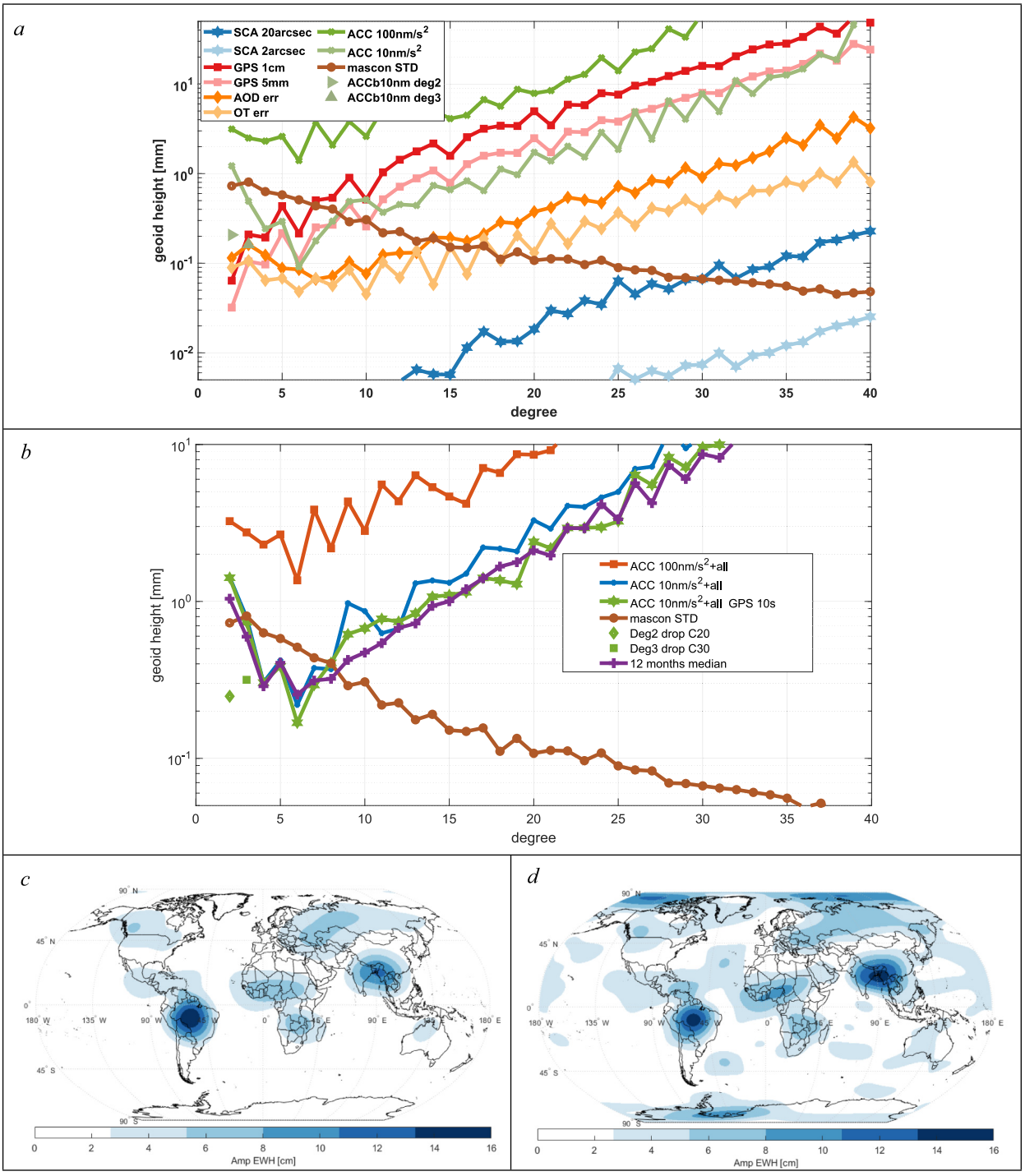

Fig. 6. Simulation results based on different error scenarios. a) Residual degree variance (DV) for each error source, e.g., the dark blue line (with asterisk) is the residual DV when we only have 20 arcsec attitude error. b) The residual DV for scenarios where we include **all** error sources. The three cases differ in GNSS sampling rate and MEMS accelerometer errors. The purple line with cross is the median residual DV for 12 monthly solution of 2008c) The ground "true" annual amplitude of mass anomalies computed from 12 monthly CSR mascon solutions in the unit of cm of equivalent water height (EWH, 1200 km Gaussian smoothing) (2008). d) Recovered annual amplitude of mass anomalies computed from 12 monthly gravity solutions (e.g. the case in green line with asterisk in b) 1200 km Gaussian smoothing).

accelerometer accuracies considered here are 2–3 orders of magnitude lower than the GRACE accelerometer. The high noise case (100 nm/s^2) is above the signal curve over the entire spectrum, which can be hardly used for the uPGRADE mission. The 10 nm/s^2 MEMS noise is very close to the effect of 5 mm GNSS noise between degree 5 and 10. The former case is slightly better for degree above 10 while worse at lower degree (below 5) due to the $1/f$ slope. This lower noise MEMS is more favorable for the uPGRADE mission considering the goal of observing tem-

poral gravity. The contributions of AOD model error and ocean tide model error (Fig. 6a, orange with diamond and light orange with diamond) are relatively lower compared to MEMS and GNSS errors. Considering the new release, version 07 AOD and the refined ocean tide model, e.g., FES2022 (Carrere et al., 2022) and GOT5.6 (Ray, 2020), we foresee that the geophysical model errors can be smaller than what we simulated here.

Fig. 6b shows the scenario with all the error sources, where 5 mm GNSS error, 20 arcsec attitude error, AOD and ocean tide error are used. In the all-error combined scenario, the case with higher MEMS accelerometer observation error (Fig. 6b red with square) has the least science value, where the accelerometer corrupts the full spectrum. Increasing the MEMS accuracy to 10 nm/s^2 clearly improves the gravity in all degrees, especially at low degrees (Fig. 6b red with square vs blue with cross). Especially considering that continental scale climate patterns are dominated by low degrees, the improvement at low degrees is very important. By increasing the sampling rate of the GNSS observation from 30 s to 10 s (Fig. 6b blue with cross vs green with asterisk), the solution is further improved for degrees above 5 by up to a factor of 2. The factor is close to the expected value of $\sqrt{3} = 1.73$ as a result of stochastic averaging of 3 times more data. However, limited by the noise level of the MEMS accelerometer (e.g., Fig. 6a light green with cross vs light red with square), the improvements in degrees 2 and 3 are insignificant by increasing the sampling rate of GNSS observations. We find the errors are mainly from C20 and C30. If we drop these two terms, the residual degree variance can drop by almost one order of magnitude (e.g., degree 2 in Fig. 6b, light green with diamond). A similar situation is also found in the real GRACE and GRACE-FO gravity field solutions, where the degraded accelerometers in the late GRACE period and the current GRACE-FO reduced the accuracy of C_{20} and C_{30} coefficients. These two coefficients are recommended to be replaced with the SLR observed value (e.g. Loomis et al., 2019, 2020). Degrees 2 and 3 are two of the most important components in monitoring the polar ice-sheet mass loss and global mean sea level change (Loomis et al., 2019, 2020). Thus, a MEMS accelerometer that has accuracy higher than the current simulation assumption is highly desired for the sake of maximizing the mission's science return.

We extended the simulation to the whole year of 2008 and estimated 12 monthly gravity solutions. The median residual DV values of these 12 solutions (Fig. 6b, purple with cross) generally algin with August 2008 (Fig. 6b, green with asterisk). Fig. 6c shows the annual amplitude of "true" mass anomalies computed from the mascon solution with 1200 km Gaussian smoothing (Jekeli, 1981; Feng, 2019). As a comparison, the annual amplitude of mass anomalies recovered from the case with 10 s sampling rate GNSS observation (Fig. 6b, light green with diamond) are shown in Fig. 6d. Under this simulation scenario, it is possible to detect the major hydrological signals at the regional scale, such as the large annual fluctuation of Amazon basin and the monsoon season of the Bangladesh delta. As we mentioned before, the relatively high noise at low degrees also presented as undesired higher noise levels near polar regions. In summary, the uPGRADE mission has the potential to recover temporal gravity up to degree 15 under the current hypothetical error budgets.

6. Summary

GRACE and the ongoing GRACE-FO mission have brought us tremendous new insights into the Earth system since 2002 (Rodell et al., 2018; Tapley et al., 2019; Landerer et al., 2020). The temporal gravity field models estimated from data collected by these two missions have been a unique and essential observable for studying a wide range of Earth system dynamics, such as sea level change, polar ice sheet mass balance, mountain glacier retreat, flood and drought, groundwater depletion, earthquake deformation and terrestrial water storage variation (Pail et al., 2015; Chen et al., 2022; Wiese et al., 2022). Securing a continuous temporal gravity observation and mitigating the temporal aliasing problem has been of high interest to the Earth Sciences community. It will also ensure a continuous gravimetric climate record of the complex Earth system. The high cost of the current GRACE-like mission hinders the implementation of the satellite constellations needed to achieve the increased spatial and temporal resolutions sought by the science community. It will impact the sustainability of measurement continuity in future decades. A viable approach is to miniaturize the size of the satellite to CubeSat (roughly shoebox size) to reduce the cost of gravimetric missions and use this as a first step towards achieving a nanosat version of the current dual satellite GRACE mission.

As an attempt to reach this objective, the uPGRADE project aims to produce a prototype gravimetric CubeSat based on the high-low satellite-to-satellite tracking system like CHAMP or Swarm satellites, with the cost objective of a fraction of the GRACE mission. As the primary payload of the gravimetric satellite, the project proposes to use the high-precision MEMS accelerometer for the first time, roughly the size of a 2 cm square, to measure the non-gravitational accelerations. In this study, we first reviewed the basic dynamics of the MEMS accelerometers in the satellite frame. We then discussed different MEMS configurations in terms of the number of MEMS and arrangements. We concluded that the 6 MEMS parallel arrangement is the most viable option for the uPGRADE mission. This 6 MEMS arrangement can directly observe the required non-gravitational acceleration by itself. Compared to the perpendicular case, it can additionally measure the magnitude of the angular velocity and has a lower construction complexity from the engineering point of view. To demonstrate the flexibility and adaptability

of the MEMS arrangements, we also proposed a 9 MEMS arrangement, which can directly measure both the non-gravitational accelerations and angular accelerations (not only a magnitude of the angular velocity in the 6 MEMS parallel arrangement). The latter observation is of great value for the satellite attitude reconstruction (Harvey et al., 2019, 2022).

The imperfect assembly of the MEMS accelerometers may result in orientation (misalignment) and position (offset) errors. Based on certain assumptions and simulations (section 4), we designed a measurement error model that is associated with orientation and position error. The error model provided a clear guideline on the minimum construction requirement with a given desired measurement accuracy.

Finally, we conducted an uPGRADE simulation study using a selection of error sources for August 2008. We found that the GNSS observation error is one of the dominant error sources for gravity inversion. The impact of 10 nm/s^2 MEMS observation error ($\gamma = 10^{-16}$) is very close to 5 mm GNSS error. However, its effect at the low degrees is much more prominent, which ends up degrading the low-degree coefficients. The C20 and C30 coefficients are particularly sensitive and affected by the MEMS error. We extended the simulation to the whole year of 2008 under the realistic assumptions where we have 5 mm GNSS error with 10-second sampling rate, 20 arcsec attitude error, 10 nm/s^2 accelerometer error, and both AOD and OT errors. Based on the simulation results, the uPGRADE mission has the potential to recover temporal gravity up to degree 15 and observe some of the major hydrological signals at the regional scale, such as the large annual fluctuation of Amazon basin and the monsoon season of the Bangladesh delta, though with compromised accuracy at high latitudes. Considering the high science value of low degrees at high latitude, we will keep working on pushing down the current projected MEMS accelerometer noise floor and increasing the science return of the uPGRADE mission.

Declaration of competing interest

The authors declare that they have no known competing financial interests or personal relationships that could have appeared to influence the work reported in this paper.

Acknowledgments

We thank NASA JPL for making the GRACE and GRACE-FO L1B data publicly accessible via PO.DDAC (https://podaac.jpl.nasa.gov/dataset/GRACE_L1B_GRAV_JPL_RL03). The authors acknowledge the Texas Advanced Computing Center (TACC) at The University of Texas at Austin for providing computational resources that have contributed to the research results reported within this paper. URL: http://www.tacc.utexas.edu. This study is supported by COMPETE 2030 & FEDER (No. COMPETE2030-FEDER-01204200) and UT Austin Portugal Program.

Open research

GRACE and GRACE-FO L1B data publicly accessible via PO.DDAC (https://podaac.jpl.nasa.gov/dataset/GRACE_L1B_GRAV_JPL_RL03). The CSR Mascon solutions in spherical harmonic representation are downloaded from https://www2.csr.utexas.edu/grace/RL06_mascons.html.

Appendix A. The observation equations for the 6 MEMS perpendicular case (Fig. 2c) are:

$$\begin{cases} A^s_{x_1} = a^s_z + \omega^s_{is_x}\cdot\omega^s_{is_z}\cdot\rho - \dot{\omega}^s_{is_y}\cdot\rho \\ A^s_{x_2} = a^s_z - \omega^s_{is_x}\cdot\omega^s_{is_z}\cdot\rho + \dot{\omega}^s_{is_y}\cdot\rho \\ A^s_{y_1} = a^s_x + \omega^s_{is_x}\cdot\omega^s_{is_y}\cdot\rho - \dot{\omega}^s_{is_z}\cdot\rho \\ A^s_{y_2} = a^s_x - \omega^s_{is_x}\cdot\omega^s_{is_y}\cdot\rho + \dot{\omega}^s_{is_z}\cdot\rho \\ A^s_{z_1} = a^s_y + \omega^s_{is_y}\cdot\omega^s_{is_z}\cdot\rho - \dot{\omega}^s_{is_x}\cdot\rho \\ A^s_{z_2} = a^s_y - \omega^s_{is_y}\cdot\omega^s_{is_z}\cdot\rho + \dot{\omega}^s_{is_x}\cdot\rho \end{cases}, \tag{A1}$$

where the green color highlights linear non-gravitational acceleration, purple color for the centrifugal acceleration and blue color for the tangential acceleration.

The common mode of the perpendicular case:

$$\begin{cases} a^s_z = \frac{1}{2}\left(A^s_{x_1} + A^s_{x_2}\right) \\ a^s_x = \frac{1}{2}\left(A^s_{y_1} + A^s_{y_2}\right) \\ a^s_y = \frac{1}{2}\left(A^s_{z_1} + A^s_{z_2}\right) \end{cases}. \tag{A2}$$

The differential mode of the perpendicular case:

$$\begin{cases} -A^s_{x_1} + A^s_{x_2} = -2\omega^s_{is_x}\cdot\omega^s_{is_z}\cdot\rho + 2\dot{\omega}^s_{is_y}\cdot\rho \\ -A^s_{y_1} + A^s_{y_2} = -2\omega^s_{is_x}\cdot\omega^s_{is_y}\cdot\rho + 2\dot{\omega}^s_{is_z}\cdot\rho \\ -A^s_{z_1} + A^s_{z_2} = -2\omega^s_{is_y}\cdot\omega^s_{is_z}\cdot\rho + 2\dot{\omega}^s_{is_x}\cdot\rho \end{cases}. \tag{A3}$$

The observation equations of 9 MEMS configuration (Fig. 2d) are:

$$\begin{cases} A^s_{x_1} = a^s_z + \omega^s_{is_x}\cdot\omega^s_{is_z}\cdot\rho_1 + \omega^s_{is_y}\cdot\omega^s_{is_z}\cdot\rho_2 + \dot{\omega}^s_{is_x}\cdot\rho_2 - \dot{\omega}^s_{is_y}\cdot\rho_1 \\ A^s_{x_2} = a^s_z + \omega^s_{is_x}\cdot\omega^s_{is_z}\cdot\rho_1 - \omega^s_{is_y}\cdot\omega^s_{is_z}\cdot\rho_2 - \dot{\omega}^s_{is_x}\cdot\rho_2 - \dot{\omega}^s_{is_y}\cdot\rho_1 \\ A^s_{x_3} = a^s_z - \omega^s_{is_x}\cdot\omega^s_{is_z}\cdot\rho_1 + \omega^s_{is_y}\cdot\omega^s_{is_z}\cdot\rho_2 + \dot{\omega}^s_{Si_x}\cdot\rho_2 + \dot{\omega}^s_{is_y}\cdot\rho_1 \\ A^s_{y_1} = a^s_x + \omega^s_{is_x}\cdot\omega^s_{is_y}\cdot\rho_1 + \omega^s_{is_x}\cdot\omega^s_{is_z}\cdot\rho_2 + \dot{\omega}^s_{is_y}\cdot\rho_2 - \dot{\omega}^s_{is_z}\cdot\rho_1 \\ A^s_{y_2} = a^s_x + \omega^s_{is_x}\cdot\omega^s_{is_y}\cdot\rho_1 - \omega^s_{is_x}\cdot\omega^s_{is_z}\cdot\rho_2 - \dot{\omega}^s_{is_y}\cdot\rho_2 - \dot{\omega}^s_{is_z}\cdot\rho_1 \\ A^s_{y_3} = a^s_x - \omega^s_{is_x}\cdot\omega^s_{is_y}\cdot\rho_1 + \omega^s_{is_x}\cdot\omega^s_{is_z}\cdot\rho_2 + \dot{\omega}^s_{is_y}\cdot\rho_2 + \dot{\omega}^s_{is_z}\cdot\rho_1 \\ A^s_{z_1} = a^s_y + \omega^s_{is_y}\cdot\omega^s_{is_z}\cdot\rho_1 + \omega^s_{is_x}\cdot\omega^s_{is_y}\cdot\rho_2 + \dot{\omega}^s_{is_z}\cdot\rho_2 - \dot{\omega}^s_{is_x}\cdot\rho_1 \\ A^s_{z_2} = a^s_y + \omega^s_{is_y}\cdot\omega^s_{is_z}\cdot\rho_1 - \omega^s_{is_x}\cdot\omega^s_{is_y}\cdot\rho_2 - \dot{\omega}^s_{is_z}\cdot\rho_2 - \dot{\omega}^s_{is_x}\cdot\rho_1 \\ A^s_{z_3} = a^s_y - \omega^s_{is_y}\cdot\omega^s_{is_z}\cdot\rho_1 + \omega^s_{is_x}\cdot\omega^s_{is_y}\cdot\rho_2 + \dot{\omega}^s_{is_z}\cdot\rho_2 + \dot{\omega}^s_{is_x}\cdot\rho_1 \end{cases}, \tag{A4}$$

$\rho_1 = 2\rho_2$

Differential mode yields:

$$\begin{cases} A^s_{x_1} - A^s_{x_3} = 2\omega^s_{Si_x}\cdot\omega^s_{Si_z}\cdot\rho_1 - 2\dot{\omega}^s_{Si_y}\cdot\rho_1 \\ A^s_{x_1} - A^s_{x_2} = \omega^s_{Si_y}\cdot\omega^s_{Si_z}\cdot\rho_1 + \dot{\omega}^s_{Si_x}\cdot\rho_1 \\ A^s_{y_1} - A^s_{y_3} = 2\omega^s_{Si_x}\cdot\omega^s_{Si_y}\cdot\rho_1 - 2\dot{\omega}^s_{Si_z}\cdot\rho_1 \\ A^s_{y_1} - A^s_{y_2} = \omega^s_{Si_x}\cdot\omega^s_{Si_z}\cdot\rho_1 + \dot{\omega}^s_{Si_y}\cdot\rho_1 \\ A^s_{z_1} - A^s_{z_3} = 2\omega^s_{Si_y}\cdot\omega^s_{Si_z}\cdot\rho_1 - 2\dot{\omega}^s_{Si_x}\cdot\rho_1 \\ A^s_{z_1} - A^s_{z_2} = \omega^s_{Si_x}\cdot\omega^s_{Si_y}\cdot\rho_1 + \dot{\omega}^s_{Si_z}\cdot\rho_1 \end{cases}, \tag{A5}$$

The linear combinations of the equation A(5) can isolate the angular acceleration:

$$\begin{cases} \dot{\omega}^s_{Si_y} = \frac{1}{4\rho_1}\left(2\left(A^s_{y_1} + A^s_{y_3}\right) - \left(A^s_{x_1} + A^s_{x_3}\right) - 2\left(A^s_{y_2} + A^s_{y_3}\right)\right) \\ \dot{\omega}^s_{Si_z} = \frac{1}{4\rho_1}\left(2\left(A^s_{z_1} + A^s_{z_3}\right) - \left(A^s_{y_1} + A^s_{y_3}\right) - 2\left(A^s_{z_2} + A^s_{z_3}\right)\right) \\ \dot{\omega}^s_{Si_x} = \frac{1}{4\rho_1}\left(2\left(A^s_{x_1} + A^s_{x_3}\right) - \left(A^s_{z_1} + A^s_{z_3}\right) - 2\left(A^s_{x_2} + A^s_{x_3}\right)\right) \end{cases} or$$

$$\begin{cases} \dot{\omega}^s_{Si_y} = \frac{1}{4\rho_1}\left(2\left(A^s_{y_1} - A^s_{y_2}\right) - \left(A^s_{x_1} - A^s_{x_3}\right)\right) \\ \dot{\omega}^s_{Si_z} = \frac{1}{4\rho_1}\left(2\left(A^s_{z_1} - A^s_{z_2}\right) - \left(A^s_{y_1} - A^s_{y_3}\right)\right) \\ \dot{\omega}^s_{Si_x} = \frac{1}{4\rho_1}\left(2\left(A^s_{x_1} - A^s_{x_2}\right) - \left(A^s_{z_1} - A^s_{z_3}\right)\right) \end{cases}. \tag{A6}$$

Appendix B. Generate colored noise with a given PSD.

Given a standardized white noise $N(1,0)$ and its DFT (FFT) pair,

$y(t) \leftrightarrow Y(f)$,

the PSD of the noise (N points, Δt sampling rate) is

$$S = \frac{\Delta t}{N} Y \cdot Y^*.$$

If the colored noise is defined as a new PSD as

$S_e = Y_e \cdot Y_e^*$

We know the PSD of a white noise is constant. Specifically

$$\frac{S}{\Delta t} = \frac{1}{N} Y \cdot Y^* = 1(\text{vector of} 1)$$

Thus, if we multiple $Y(f)$ with $\frac{|Y_e|}{\Delta t^{1/2}}$, we have the new colored noise

$w(t) \leftrightarrow W(f)$

$$W(f) = Y \cdot \frac{|Y_e|}{\Delta t^{\frac{1}{2}}}$$

The new PSD is $\frac{\Delta t}{N} Y \cdot Y^* \frac{Y_e \cdot Y_e^*}{\Delta t} = S_e$. Now we can take the inverse DFT (FFT) of $W(f)$ to get the colored noise $w(t)$.

Fig. B1 shows an example of the PSD in Equation (13), where two floor variances 10 nm/s^2 and 100 nm/s^2 are used.

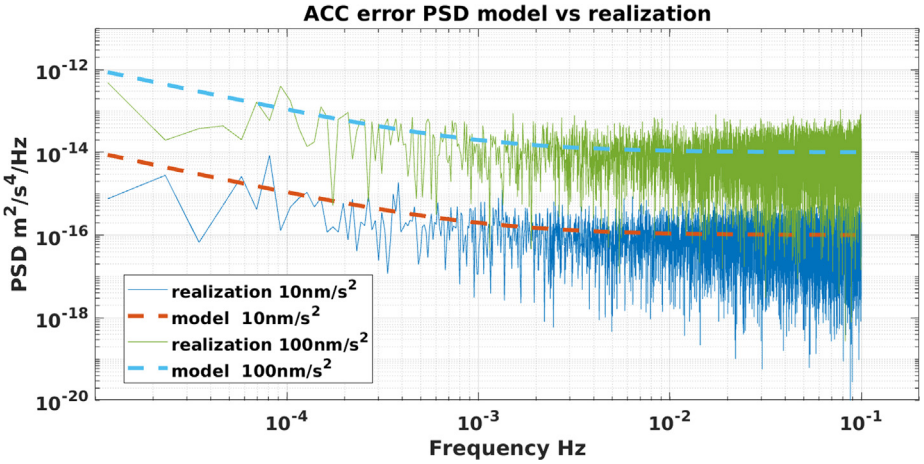

Fig. B1 MEMS measurement error realization using Equation . Red and cyan dash are models based on 10 nm/s^2 and 100 nm/s^2 floor variance. Blue and green are realized acceleration errors for these two cases.

References

Bao, Y., Cervantes, F.G., Balijepalli, A., Lawall, J.R., Taylor, J.M., LeBrun, T.W., Gorman, J.J., 2016. An optomechanical accelerometer with a high-finesse hemispherical optical cavity. IEEE Int. Symp. Inertial Sens. Syst. 2016, 105–108. https://doi.org/10.1109/ISISS.2016.7435556.

Bender, P.L., Conklin, J.W., Wiese, D.N., 2025. Short-period mass variations and the next generation gravity mission. J. Geophys. Res. Solid Earth 130 (1). https://doi.org/10.1029/2024JB030290 e2024JB030290.

Bezděk, A., Sebera, J., Teixeira da Encarnação, J., Klokočník, J., 2016. Time-variable gravity fields derived from GPS tracking of Swarm. Geophys. J. Int. 205 (3), 1665–1669. https://doi.org/10.1093/gji/ggw094.

Boulanger, D., Christophe, B., Lebat, V., Liorzou, F., Maquaire, K., Portier, N., Rodrigues, M. 2024. CubeSTAR: A tiny space accelerometer for Earth Observation applications. 4S Symposium 2024. https://hal.science/hal-04893354.

Brockmann, J.M., Schubert, T., Schuh, W.-D., 2021. An improved model of the earth's static gravity field solely derived from reprocessed GOCE data. Surv. Geophys. 42 (2), 277–316. https://doi.org/10.1007/s10712-020-09626-0.

Carrere, L., Lyard, F., Cancet, M., Allain, D., Dabat, M.-L., Fouchet, E., Sahuc, E., Faugere, Y., Dibarboure, G., Picot, N., 2022. A new barotropic tide model for global ocean. FES2022. 43. https://doi.org/10.24400/527896/a03-2022.3287.

Case, K., Kruizinga, G., Wu, S.-C. 2010. GRACE Level 1B Data Product User Handbook (No. JPL D-22027). https://earth.esa.int/eogateway/documents/20142/37627/GRACE-L1B-Handbook-v1.3.pdf.

Chen, J., Cazenave, A., Dahle, C., Llovel, W., Panet, I., Pfeffer, J., Moreira, L., 2022. Applications and challenges of GRACE and GRACE follow-on satellite gravimetry. Surv. Geophys. 43 (1), 305–345. https://doi.org/10.1007/s10712-021-09685-x.

Conklin, J.W., Apple, S., Álvarez, A.D., Bennett, S., Bevilacqua, R., Bischof, L., Conroy, J., Footdale, J., Forrester, Z., Fulda, P., Hanson, J., Hollis, H., Kennedy, V., Kinzie, R., Perkins, C., Sanjuan, J., Schwarze, T., Siu, J., Spero, R., et al. 2025. GRATTIS: The gravitational reference advanced technology test in space. Small Satellites Systems and Services Symposium (4S 2024), 13546, 925–937. https://doi.org/10.1117/12.3061925.

Dobslaw, H., Bergmann-Wolf, I., Dill, R., Poropat, L., Thomas, M., Dahle, C., Esselborn, S., König, R., Flechtner, F., 2017. A new high-resolution model of non-tidal atmosphere and ocean mass variability for de-aliasing of satellite gravity observations: AOD1B RL06. Geophys. J. Int. 211 (1), 263–269. https://doi.org/10.1093/gji/ggx302.

Esteves, D., Hormigo, T., Encarnação, J., Dias, R. A., Neves, D., Oliveira, J., Câmara, F. 2022. Miniaturized prototype for gravity field assessment using distributed earth-orbiting assets. Small Satellites Systems and Services Symposium (4S 2022). https://airdrive.eventsair.com/eventsairwesteuprod/production-atpi-public/787589b589e2446796e6457fd9db488b.

Feng, W., 2019. GRAMAT: a comprehensive Matlab toolbox for estimating global mass variations from GRACE satellite data. Earth Sci. Inf. 12 (3), 389–404. https://doi.org/10.1007/s12145-018-0368-0.

Flechtner, F., Reigber, C., Rummel, R., Balmino, G., 2021. Satellite gravimetry: a review of its realization. Surv. Geophys. 42 (5), 1029–1074. https://doi.org/10.1007/s10712-021-09658-0.

Frommknecht, B., Lamarre, D., Meloni, M., Bigazzi, A., Floberghagen, R., 2011. GOCE level 1b data processing. J. Geod. 85 (11), 759–775. https://doi.org/10.1007/s00190-011-0497-4.

Garcia, I.S., Elhawash, A., Cabral, J., Hormigo, T., DaEncarnação, J., Alves, F., Dias, R., 2022. Ultra-low noise, high-sensitivity mems accelerometer for satellite gravimetry. 2022 Solid-State, Actuators, and Microsystems Workshop Technical Digest, 391–394. https://doi.org/10.31438/trf.hh2022.97.

Garcia, I.S.M. 2019. High precision MEMS accelerometer for microsatellites (Ph.D. thesis). https://hdl.handle.net/1822/64779.

Gunter, B., Ries, J., Bettadpur, S., Tapley, B., 2006. A simulation study of the errors of omission and commission for GRACE RL01 gravity fields. J. Geod. 80 (7), 341–351. https://doi.org/10.1007/s00190-006-0083-3.

Guzman, F., Sanjuan, J., 2024. ODIN – Optomechanical-distributed instrument for Inertial sensing and Navigation (Nos. GSTM2024-43). GSTM2024). Copernicus Meetings. https://doi.org/10.5194/gstm2024-43.

Harvey, N., Sakumura, C., 2019. Results from a GRACE/GRACE-FO attitude reconstruction Kalman filter. J. Geod. 93 (10), 1881–1896. https://doi.org/10.1007/s00190-019-01289-z.

Harvey, N., McCullough, C.M., Save, H., 2022. Modeling GRACE-FO accelerometer data for the version 04 release. Adv. Space Res. 69 (3), 1393–1407. https://doi.org/10.1016/j.asr.2021.10.056.

Heiskanen, W.A., Moritz, H., 1967. PhysicalGeodesy. W. H. Freeman and Company, San Francisco.

Hines, A., Nelson, A., Zhang, Y., Valdes, G., Sanjuan, J., Stoddart, J., Guzmán, F., 2022. Optomechanical accelerometers for geodesy. Remote Sens. (Basel) 14 (17), 4389. https://doi.org/10.3390/rs14174389.

Hines, A., Richardson, L., Wisniewski, H., Guzman, F., 2020. Optomechanical inertial sensors. Appl. Opt. 59 (22), G167–G174. https://doi.org/10.1364/AO.393061.

Hofmann-Wellenhof, B., Moritz, H., 2006. *Physical Geodesy*. Springer Vienna. https://doi.org/10.1007/978-3-211-33545-1.

Jekeli, C. 1981. Alternative methods to smooth the Earth's gravity field (No. 327; OSU Report). https://earthsciences.osu.edu/sites/earth-sciences.osu.edu/files/report-327.pdf.

Jekeli, C., 2001. Inertial navigation systems with geodetic applications. De Gruyter. https://doi.org/10.1515/9783110800234.

Kang, Z., Bettadpur, S., Nagel, P., Save, H., Poole, S., Pie, N., 2020. GRACE-FO precise orbit determination and gravity recovery. J. Geod. 94 (9), 85. https://doi.org/10.1007/s00190-020-01414-3.

Kang, Z., Tapley, B., Bettadpur, S., Ries, J., Nagel, P., Pastor, R., 2006. Precise orbit determination for the GRACE mission using only GPS data. J. Geod. 80 (6), 322–331. https://doi.org/10.1007/s00190-006-0073-5.

Kim, J. 2000. Simulation Study of A Low-Low Satellite-to-Satellite Tracking Mission (Ph.D. thesis, University of Texas at Austin). https://hdl.handle.net/2152/85744.

Kim, J., Tapley, B.D., 2002. Error analysis of a low-low satellite-to-satellite tracking mission. J. Guid. Control Dynam. 25 (6), 1100–1106. https://doi.org/10.2514/2.4989.

Klinger, B. 2018. A contribution to GRACE time-variable gravity field recovery: Improved level-1B data pre-processing methodologies [Ph.D. thesis, Graz University of Technology]. https://repository.tugraz.at/publications/4nwh1-24657.

Landerer, F.W., Flechtner, F.M., Save, H., Webb, F.H., Bandikova, T., Bertiger, W.I., Bettadpur, S.V., Byun, S.H., Dahle, C., Dobslaw, H., Fahnestock, E., Harvey, N., Kang, Z., Kruizinga, G.L.H., Loomis, B. D., McCullough, C., Murböck, M., Nagel, P., Paik, M., Yuan, D.-N., 2020. Extending the global mass change data record: GRACE follow-on instrument and science data performance. Geophys. Res. Lett. 47 (12). https://doi.org/10.1029/2020GL088306 e2020GL088306.

Loomis, B.D., Rachlin, K.E., Luthcke, S.B., 2019. Improved earth oblateness rate reveals increased ice sheet losses and mass-driven sea level rise. Geophys. Res. Lett. 46 (12), 6910–6917. https://doi.org/10.1029/2019GL082929.

Loomis, B.D., Rachlin, K.E., Wiese, D.N., Landerer, F.W., Luthcke, S. B., 2020. Replacing GRACE/GRACE-FO C30 with satellite laser ranging: impacts on Antarctic ice sheet mass change. Geophys. Res. Lett. 47 (3). https://doi.org/10.1029/2019GL085488 e2019GL085488.

Lyard, F., Lefevre, F., Letellier, T., Francis, O., 2006. Modelling the global ocean tides: modern insights from FES2004. Ocean Dyn. 56 (5), 394–415. https://doi.org/10.1007/s10236-006-0086-x.

National Academies of Sciences, Engineering, and Medicine. 2019. Thriving on Our Changing Planet: A Decadal Strategy for Earth Observation from Space. National Academies Press. https://doi.org/10.17226/24938.

Pail, R., Bruinsma, S., Migliaccio, F., Förste, C., Goiginger, H., Schuh, W.-D., Höck, E., Reguzzoni, M., Brockmann, J.M., Abrikosov, O., Veicherts, M., Fecher, T., Mayrhofer, R., Krasbutter, I., Sansò, F., Tscherning, C.C., 2011. First GOCE gravity field models derived by three different approaches. J. Geod. 85 (11), 819–843. https://doi.org/10.1007/s00190-011-0467-x.

Pail, R., Bingham, R., Braitenberg, C., Dobslaw, H., Eicker, A., Güntner, A., Horwath, M., Ivins, E., Longuevergne, L., Panet, I., Wouters, B. IUGG Expert Panel, 2015. Science and user needs for observing global mass transport to understand global change and to benefit society. Surveys in Geophysics 36 (6), 743–772. https://doi.org/10.1007/s10712-015-9348-9.

Pfaffenzeller, N., Pail, R., 2023. Small satellite formations and constellations for observing sub-daily mass changes in the Earth system. Geophys. J. Int. 234 (3), 1550–1567. https://doi.org/10.1093/gji/ggad132.

Pie, N., Bettadpur, S.V., Tamisiea, M., Krichman, B., Save, H., Poole, S., Nagel, P., Kang, Z., Jacob, G., Ellmer, M., Fahnestock, E., Landerer, F.W., McCullough, C., Yuan, D.-N., Wiese, D.N., 2021. Time variable earth gravity field models from the first spaceborne laser ranging interferometer. J. Geophys. Res. Solid Earth 126 (12). https://doi.org/10.1029/2021JB022392 e2021JB022392.

Pike, W.T., Calcutt, S., Standley, I.M., Mukherjee, A.G., Temple, J., Warren, T., Charalambous, C., Liu, H., Stott, A., McClean, J.B. 2016. A Silicon Seismic Package (SSP) for Planetary Geophysics. 47th Annual Lunar and Planetary Science Conference, 2081. https://www.hou.usra.edu/meetings/lpsc2016/pdf/2081.pdf.

Ray, R.D., 2020. First global observations of third-degree ocean tides. Sci. Adv. 6 (48). https://doi.org/10.1126/sciadv.abd4744 eabd4744.

Reigber, C., Lühr, H., Schwintzer, P. (Eds.). 2003. First CHAMP Mission Results for Gravity, Magnetic and Atmospheric Studies. Springer. https://doi.org/10.1007/978-3-540-38366-6.

Rim, H.J. 1992. Topex orbit determination using GPS tracking system (Ph.D., The University of Texas at Austin). https://www.proquest.com/docview/304029062/abstract/A1EAE1CF43324B36PQ/1.

Rodell, M., Famiglietti, J.S., Wiese, D.N., Reager, J.T., Beaudoing, H.K., Landerer, F.W., Lo, M.-H., 2018. Emerging trends in global freshwater availability. Nature 557 (7707), 651–659. https://doi.org/10.1038/s41586-018-0123-1.

Rodrigues, M., Bergé, J., Boulanger, D., Christophe, B., Dalin, M., Lebat, V., Liorzou, F. 2022. Space accelerometers for micro and nanosatellites: fundamental Physics and Geodesy missions from MICROSCOPE, GOCE and GFO return of experience. 4S Symposium 2022. https://hal.science/hal-03854833.

Rummel, R., Gruber, T., 2010. Gravity and steady-state ocean circulation explorer GOCE. In: Flechtner, F.M., Gruber, T., Güntner, A., Mandea, M., Rothacher, M., Schöne, T., Wickert, J. (Eds.), System Earth via Geodetic-Geophysical Space Techniques. Springer, pp. 203–212. https://doi.org/10.1007/978-3-642-10228-8_16.

Save, H., Bettadpur, S., Tapley, B.D., 2016. High-resolution CSR GRACE RL05 mascons. J. Geophys. Res. Solid Earth 121 (10), 7547–7569. https://doi.org/10.1002/2016JB013007.

Save, H. 2020. CSR GRACE and GRACE-FO RL06 Mascon Solutions v02. In: University of Texas at Austin (p. 1). https://doi.org/10.15781/cgq9-nh24.

Shihora, L., Balidakis, K., Dill, R., Dahle, C., Ghobadi-Far, K., Bonin, J., Dobslaw, H., 2022. Non-tidal background modeling for satellite gravimetry based on operational ECWMF and ERA5 reanalysis data: AOD1B RL07. J. Geophys. Res. Solid Earth 127 (8). https://doi.org/10.1029/2022JB024360 e2022JB024360.

Skachko, S., Danilov, S., Janjić, T., Schröter, J., Sidorenko, D., Savcenko, R., Bosch, W., 2008. Sequential assimilation of multi-mission dynamical topography into a global finite-element ocean model. Ocean Sci. 4 (4), 307–318. https://doi.org/10.5194/os-4-307-2008.

Smith, M. 2018. NASA's GRACE-FO, Five Iridium Satellites Share A Ride to Space. https://spacepolicyonline.com/news/nasas-grace-fo-five-iridium-satellites-share-a-ride-to-space/.

Stummer, C.S. 2012. Gradiometer Data Processing and Analysis for the GOCE Mission (Ph.D. thesis, Technical University of Munich). https://mediatum.ub.tum.de/doc/1111698/362238.pdf.

Tapley, B.D., Bettadpur, S., Ries, J.C., Thompson, P.F., Watkins, M.M., 2004. GRACE measurements of mass variability in the earth system. Science 305 (5683), 503–505. https://doi.org/10.1126/science.1099192.

Tapley, B.D., Watkins, M.M., Flechtner, F., Reigber, C., Bettadpur, S., Rodell, M., Sasgen, I., Famiglietti, J.S., Landerer, F.W., Chambers, D. P., Reager, J.T., Gardner, A.S., Save, H., Ivins, E.R., Swenson, S.C., Boening, C., Dahle, C., Wiese, D.N., Dobslaw, H., Velicogna, I., 2019. Contributions of GRACE to understanding climate change. Nat. Clim. Chang. 9 (5), 358–369. https://doi.org/10.1038/s41558-019-0456-2.

Teixeira da Encarnação, J., Visser, P., Arnold, D., Bezdek, A., Doornbos, E., Ellmer, M., Guo, J., van den IJssel, J., Iorfida, E., Jäggi, A., Klokocník, J., Krauss, S., Mao, X., Mayer-Gürr, T., Meyer, U., Sebera, J., Shum, C.K., Zhang, C., Zhang, Y., Dahle, C., 2020. Description of the multi-approach gravity field models from Swarm GPS data. Earth Syst. Sci. Data 12 (2), 1385–1417. https://doi.org/10.5194/essd-12-1385-2020.

Wang, Q., Li, Z., Liu, H., Xu, Q., Yan, S., Zhang, L., Zhang, S., Song, X., Qu, Z., Liu, L., Liu, J., Tu, L., 2021. MEMS microgravity measurement module with nano-g/Hz noise floor for spaceborne higher-level microgravity scientific experiment applications. ACS Appl. Electron. Mater. 3 (8), 3379–3390. https://doi.org/10.1021/acsaelm.1c00359.

Weigelt, M., van Dam, T., Jäggi, A., Prange, L., Tourian, M.J., Keller, W., Sneeuw, N., 2013. Time-variable gravity signal in Greenland revealed by high-low satellite-to-satellite tracking. J. Geophys. Res. Solid Earth 118 (7), 3848–3859. https://doi.org/10.1002/jgrb.50283.

Wen, H.Y., Kruizinga, G., Paik, M., Landerer, F., Mccullough, C., 2019. GRACE-FO level-1 data product user handbook. JPL Publication D-56935. https://podaacjpl.nasa.gov/dataset/GRACEFO_L1B_ASCII_GRAV_JPL_RL04.

Wiese, D.N. 2020. The NASA Mass Change Designated Observable Study: Status Update. GRACE-FO Science Team Meeting 2020. https://smd-cms.nasa.gov/wp-content/uploads/2023/05/MC_GSTM2021_offline_presentation.pdf.

Wiese, D.N., Bienstock, B.J., Bearden, D., Boening, C., Case, K.E., Chrone, J., et al. 2021. Results from the NASA Mass Change Designated Observable Study. GRACE-FO Science Team Meeting 2021. https://smd-cms.nasa.gov/wp-content/uploads/2023/05/MC_GSTM2021_offline_presentation.pdf.

Xiao, Y., Yang, Y., Pan, Z., Liu, X., Sun, Z., 2023. Performance and application of the Chinese satellite-to-satellite tracking gravimetry system. Chin. Sci. Bull. 68, 2655–2664. https://doi.org/10.1360/TB-2022-1057.

Yang, H., Yu, Z., Li, X., Wang, Y., 2005. A novel pull-in accelerometer based on cantilever beam mass structure. 2005 IEEE SENSORS 4, pp.-. https://doi.org/10.1109/ICSENS.2005.1597781.

Zemp, M., Chao, Q., Han Dolman, A.J., Herold, M., Krug, T., Speich, S., et al. 2022. Gcos 2022 implementation plan. https://gcos.wmo.int/site/global-climate-observing-system-gcos/publications.

Zhang, C., Shum, C.K., Bezděk, A., Bevis, M., de Teixeira da Encarnação, J., Tapley, B.D., Zhang, Y., Su, X., Shen, Q., 2021. Rapid mass loss in west Antarctica revealed by swarm gravimetry in the absence of GRACE. Geophys. Res. Lett. 48 (23). https://doi.org/10.1029/2021GL095141 e2021GL095141.

Zhou, H., Zhou, Z., Luo, Z., Wang, K., Wei, M., 2020. What can be expected from GNSS tracking of satellite constellations for temporal gravity field model determination?. Geophys. J. Int. 222 (1), 661–677. https://doi.org/10.1093/gji/ggaa177.